

RESEARCH ARTICLE

Experimental operation of a solar-driven climate system with thermal energy storages using mixed-integer nonlinear model predictive control

Adrian Bürger^{1,2,3}  | Daniel Bull¹  | Parantapa Sawant⁴  |
 Markus Bohlayer^{2,5} | Andreas Klotz¹ | Daniel Beschütz¹ |
 Angelika Altmann-Dieses^{1,2} | Marco Braun^{1,2} | Moritz Diehl^{3,6}

¹Faculty of Management Science and Engineering, Karlsruhe University of Applied Sciences, Karlsruhe, Germany

²Institute of Refrigeration, Air-Conditioning, and Environmental Engineering (IKKU), Karlsruhe University of Applied Sciences, Karlsruhe, Germany

³Systems Control and Optimization Laboratory, Department of Microsystems Engineering (IMTEK), University of Freiburg, Freiburg im Breisgau, Germany

⁴Institute of Energy Systems Technology (INES), Offenburg University of Applied Sciences, Offenburg, Germany

⁵Professorship of Economics (Industrial Organization and Energy Markets), Friedrich-Alexander-Universität Erlangen-Nürnberg, Nürnberg, Germany

⁶Department of Mathematics, University of Freiburg, Freiburg im Breisgau, Germany

Correspondence

Adrian Bürger, Institute of Refrigeration, Air-Conditioning, and Environmental Engineering (IKKU), Karlsruhe University of Applied Sciences, Moltkestraße 30, 76133 Karlsruhe, Germany.
 Email: adrian.buerger@hs-karlsruhe.de

Funding information

Bundesministerium für Umwelt, Naturschutz und nukleare Sicherheit, Grant/Award Number: 03KF0094A; Bundesministerium für Wirtschaft und

Abstract

This work presents the results of experimental operation of a solar-driven climate system using mixed-integer nonlinear model predictive control (MPC). The system is installed in a university building and consists of two solar thermal collector fields, an adsorption cooling machine with different operation modes, a stratified hot water storage with multiple inlets and outlets as well as a cold water storage. The system and the applied modeling approach is described and a parallelized algorithm for mixed-integer nonlinear MPC and a corresponding implementation for the system are presented. Finally, we show and discuss the results of experimental operation of the system and highlight the advantages of the mixed-integer nonlinear MPC application.

KEYWORDS

experimental study, mixed-integer nonlinear programming, model predictive control, renewable energy systems, solar thermal climate systems

Energie, Grant/Award Numbers:
0324125B, 0324166B; Deutsche
Forschungsgemeinschaft, Grant/Award
Number: Research Unit FOR 2401;
INTERREG V Upper Rhine, Grant/Award
Number: Project ACA-MODES;
Ministerium für Wissenschaft, Forschung
und Kunst Baden-Württemberg,
Grant/Award Number: Az:
22-7533.-30-20/9/3; Reiner
Lemoine-Stiftung, Grant/Award Number:
1581440000956

1 | INTRODUCTION

The development of powerful control strategies for renewable energy systems is an important task, as these can increase the efficiency of such systems, support their integration into the current supply systems, and with this, support the transition toward a sustainable energy supply. In particular, model predictive control (MPC) has been shown to be suitable for control of such systems and demonstrated on various applications, for example, for microgrids,^{1,2} heat pump systems,³ energy systems in low energy buildings,^{4,5} and solar power plants.^{6,7}

Within MPC-based control strategies, a model of the controlled system is used to determine a sequence of control signals which are optimal for system operation regarding a defined control objective for a given time horizon, while explicitly considering system dynamics, state and control boundaries, and the current system state.⁸ With this, MPC enables the identification of predictive and situation-dependent and individual control decisions⁹ as well as the direct incorporation of forecasts for demands¹⁰ and driving energy availability.¹¹ These properties are favorable for operation of renewable energy systems, which on the one hand often depend on external and immutable factors such as solar power and wind,¹² and on the other hand can include different storage technologies.¹³ This often renders MPC advantageous for control of such systems in comparison to conventional, rule-based control strategies, cf. References 14 and 15.

Application of MPC requires the solution of optimization problems within real-time suitable time scales. As energy systems often include components that show switching behavior, MPC in this context typically requires the fast solution of mixed-integer optimization problems. These are typically formulated as either mixed-integer linear programs (MILPs) or mixed-integer quadratic programs (MIQPs) to facilitate sufficiently fast solutions of these problems. Examples of simulation studies can be found for multicriteria optimal operation of a microgrid¹⁶ and mixed-integer MPC of variable-speed heat pumps.¹⁷ Examples of experimental studies are the exergy-based control of a heat exchanger within an energy supply system,¹⁸ experimental operation of a microgrid,¹⁹ and control of heating, ventilation, and air conditioning (HVAC) systems²⁰ and heating systems²¹ of buildings.

The use of linear(ized) modeling for MPC of energy systems yields several advantages, such as the availability of efficient solution methods and software, as well as the existence of certain guarantees regarding the optimality of the obtained solution, cf. Reference 22. However, the underlying processes are often characterized by nonlinear correlations. For example, nonlinearities arise from the incorporation of nonlinear coefficient of performance (COP) considerations, utilization of mass flows as control variables in models based on the first law of thermodynamics, or nonlinear distributions of mass flows between components as a function of a pump and mixing valve operation. Due to that, the use of nonlinear modeling facilitates improved system descriptions, which in turn could further improve the control decisions for a system. However, utilization of nonlinear models of switched systems in this context typically gives rise to mixed-integer nonlinear programs (MINLPs), which are hard to solve. Applications of mixed-integer nonlinear programming techniques can be found within optimal scheduling applications for energy systems, for example, for building energy systems^{23,24} and combined heat and power plants.²⁵ For application within MPC, arising MINLPs need to be solved sufficiently fast for real-time control of a considered system. For this task, application of general MINLP solvers is typically not favorable.²⁶ Instead, approaches are presented in the literature that aim at obtaining a suboptimal, however, fast and typically approximate solution of the original MINLP, cf. References 27–29. In a previous work,³⁰ we presented a simulation study for mixed-integer nonlinear MPC for a solar-thermal climate system using a decomposition approach presented by.^{26,31} However, the literature lacks real-life experiments in which the applicability of nonlinear MPC of switched renewable energy systems is demonstrated in real-time.

In this work, we present the real-life experimental operation of such a system installed at Karlsruhe University of Applied Sciences using mixed-integer nonlinear MPC. The system consists of solar thermal collector fields, an adsorption cooling machine (ACM) with different operation modes, a stratified hot water storage with multiple inlets and outlets as well as a cold water storage. Utilized for air conditioning of a part of the university building, the system operates under real conditions. As the system shows highly nonlinear behavior, complex component interaction, delays, and strong dependencies on external factors such as solar irradiation and ambient temperature, the plant is suitable for experimental studies on mixed-integer nonlinear MPC of renewable energy systems.

The contributions of this work are as follows. First, we extend the model presented in our previous work³⁰ and provide insight on the control-oriented modeling of the solar thermal collector fields, which are connected in parallel and show a nonlinear mass flow distribution as a function of pump and mixing valve operation, as well as on the modeling of the stratified hot water storage with multiple inlets and outlets. Then, we introduce a parallelized and modified version of the algorithm for mixed-integer nonlinear MPC used in our previous simulation study³⁰ that enables faster updates of control decisions and apply strategies for further decrease of algorithm runtime. Finally, we present and discuss experimental results of real-time MPC operation for the physical system on a day with challenging operation conditions and highlight the advantages of mixed-integer nonlinear MPC application for the system.

The remainder of this work is organized as follows. In Section 2, the solar thermal climate system subject to this study is introduced, followed by a description of a control-oriented nonlinear model for the system in Section 3. The mixed-integer nonlinear optimal control problem (OCP) for the system and a corresponding moving horizon estimation (MHE) problem for state estimation are presented in Section 4, including a description of the applied solution methods, MPC algorithm, and a selection of important implementation details. Finally, in Section 5, the results of experimental operation of the system are shown and discussed. Section 6 concludes this article.

2 | DESCRIPTION OF THE SOLAR THERMAL CLIMATE SYSTEM

The system considered for this study is a solar-thermally-driven climate system installed at the Faculty of Management Science and Engineering at Karlsruhe University of Applied Sciences. The system is operated for covering cooling loads of the building's atrium during summer time and for heating support during winter time. Within this study, we will focus on summer operation, which is the more comprehensive case as it involves operation of more system components compared to winter operation and in particular switching of the ACM. A more detailed description of the system and its components is given in the upcoming sections.

2.1 | Adsorption cooling machine

The central component of the system is a silica-gel/water ACM which is located in the cellar of the building, see Figure 1. The ACM is connected to a recooling tower (RT) on the roof of the building which is operated in a frost-proof circuit, see Figure 2, via a heat exchanger in the cellar further entitled as recooling tower heat exchanger (RTHX). The ACM can operate in three different modes, which can only be switched on or off completely and whereof at most one mode can be active at a time. Operation of the machine internal pumps and valves as well as the RT pump and fan speeds for each mode are subject to a dedicated internal controller of the ACM.*

Running in *adsorption cooling (AC) mode* ($b_{ac} = 1$), the ACM utilizes the heat from a stratified high-temperature storage (HTS) with volume $V_{hts} = 2 \text{ m}^3$ to cool down a stratified low-temperature storage (LTS) with volume $V_{lts} = 1 \text{ m}^3$, heat is emitted through the RT. In this mode, cooling power and COP of an ACM depend on the inlet temperatures of the three circuits of the machine, while higher high temperature (HT)- and low temperature (LT)- and lower recooling-temperatures are favorable.³³

In times of low ambient temperature, the machine can run in a *free cooling (FC) mode* ($b_{fc} = 1$), which allows to cool down the LTS via the RT. Using the third mode, which is entitled *emergency cooling (EC) mode* ($b_{ec} = 1$), the ACM can be utilized to cool down the HTS at the ambient via the RT to prevent overheating of the HTS, and with this, overheating of the solar collectors.

*While we focus on the optimal switching of an ACM within this work, it should be noted that MPC can also yield large potential for optimization of the internal processes of an ACM.³²

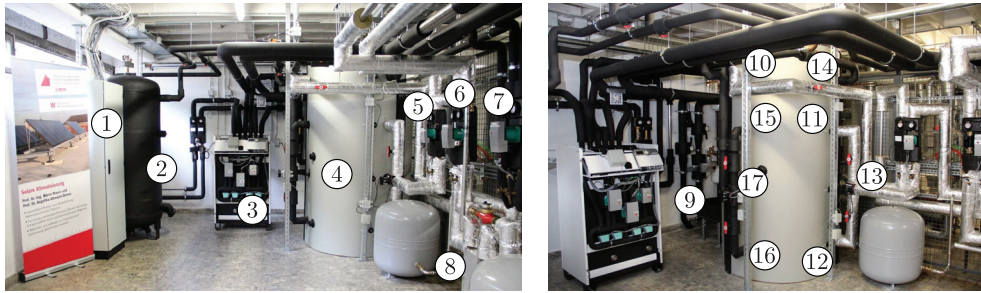


FIGURE 1 System components in the cellar of the building: (1) control cabinet, (2) low temperature storage, (3) adsorption cooling machine, (4) high temperature storage, (5) pump P_{ssc} , (6) pump P_{psc} , (7) pump P_{lc} , (8) solar heat exchanger, (9) recooling tower heat exchanger, (10) inlet $I_{hts,t}$, (11) outlet $O_{hts,m}$, (12) outlet $O_{hts,b}$, (13) mixing valve M_{ssc} , (14) outlet $O_{hts,t}$, (15) inlet $I_{hts,m}$, (16) inlet $I_{hts,b}$, (17) mixing valve M_{acm}



FIGURE 2 System components on the roof of the building: (1) vacuum tube solar collectors, (2) sensor T_{vtsc} , (3) flat plate solar collectors, (4) sensor T_{fpssc} , (5) recooling tower, (6) pyranometer and ambient temperature sensor

The temperature at the inlets and outlets of the ACM and the current flows in each circuit are measured, as well as the temperatures at the inlets and outlets of the RTHX and the outlet temperature of the RT.

2.2 | High-temperature circuits

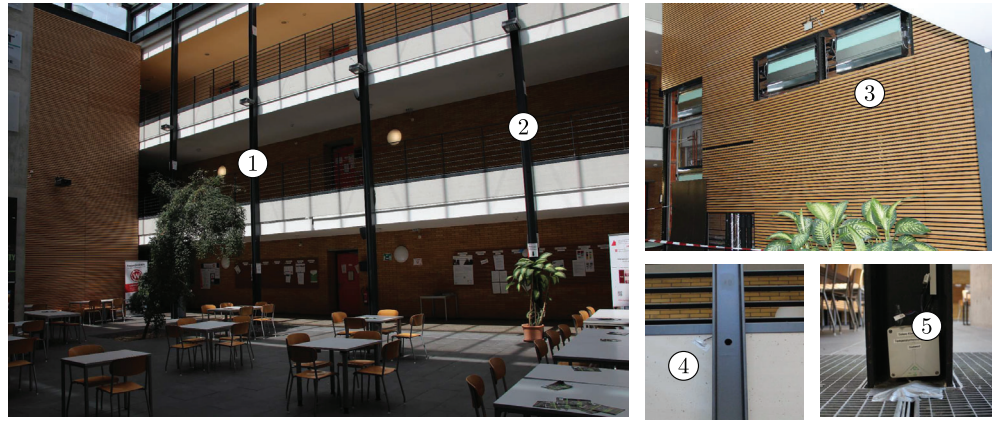
The heat stored in the HTS is collected by two roof-top solar thermal collector arrays as shown in Figure 2. One array consists of horizontally placed vacuum tube solar collectors (VTSC) with total area $A_{vtsc} = 31.2 \text{ m}^2$ and the other consists of flat plate solar collectors (FPSC) with total area $A_{fpssc} = 53.3 \text{ m}^2$ mounted at a 45° angle facing south.

Both arrays are connected to a circuit entitled primary solar circuit (PSC) with approximate volume $V_{psc} = 0.4 \text{ m}^3$. The PSC is filled with an anti-freeze brine and is separated from the indoor water circuits by a solar heat exchanger (SHX) located in the cellar, see Figure 1. The amount of liquid flowing through the PSC and the individual collector arrays can be controlled by modulating the speed v_{ppsc} of the pump P_{psc} and the position p_{mpsc} of the mixing valve M_{psc} which is located in the return line of the PSC. The water-filled circuit on the other side of the SHX is entitled the secondary solar circuit (SSC) and is directly connected to the HTS. The amount of liquid flowing through the SSC can be controlled by modulating the speed v_{pssc} of the pump P_{ssc} .

Water returning from the SHX to the HTS in the SSC is always supplied into the top inlet $I_{hts,t}$ of the HTS as shown in Figure 1. However, the water flowing toward the SHX can be extracted from the middle outlet $O_{hts,m}$, the bottom outlet $O_{hts,b}$, or a combination of both, depending on the position p_{mssc} of the mixing valve M_{ssc} . For hot water supply of the ACM the top outlet $O_{hts,t}$ of the HTS is used. The water returning from the ACM to the HTS can be inserted into the middle inlet $I_{hts,m}$, the bottom inlet $I_{hts,b}$, or a combination of both, depending on the position p_{macm} of the mixing valve M_{acm} .

The temperature sensors T_{vtsc} and T_{fpssc} for the collector arrays are installed directly at the array outlets in the return line of the PSC. Therefore, the array temperatures can not be measured directly, but only via the temperature of the medium returning from the arrays, that is, only when P_{psc} is operating. Additionally, the ambient temperature and the current solar irradiation on the roof are measured using a temperature sensor T_{amb} and a pyranometer I_g , respectively. Further, the temperatures at each inlet and outlet of the SHX are measured using the sensors $T_{shx,psc,i}$, $T_{shx,psc,o}$, $T_{shx,ssc,i}$

FIGURE 3 System components in the atrium of the building: (1) location of installation North-West, (2) location of installation North-East, (3) fan coil units, (4) sensor for measurement of concrete temperature, and (5) detail view of installation South-West



and $T_{shx,ssc,o}$. Also, the inlet and outlet temperature of the HTS can be monitored, as well as the flows in each circuit. Each mixing valve is equipped with a potentiometer which allows to determine the valve's current position. Also, $n_{hts} = 4$ temperature sensors $T_{hts,k}$, $k = 1, \dots, n_{hts}$ are inserted into thermometer pockets installed at different heights of the HTS.

2.3 | Low-temperature circuits and room installations

The atrium of the building, which is depicted in Figure 3, has a length of $l_{atrium} = 17.2$ m and width of $w_{atrium} = 11$ m. With a height of $h_{atrium} = 12.7$ m, the room extends over three floors. The glass roof of the atrium can be covered using outdoor blinds, which are typically closed during summer and cover most of the glass surface.

Behind the plumbing wall covered by wooden panels, four fan coil units (FCUs) are installed as shown in Figure 3. These are supplied by chilled water from the bottom of the LTS, which is then returned from the FCUs into the top of the LTS. This circuit is entitled the load circuit (LC) and the medium flowing through this circuit can be controlled by modulating the speed v_{plc} of the pump P_{lc} .[†]

On four of the depicted black steel beams, installations for temperature measurement are attached, see Figure 3. According to their locations, these are labeled North-West (NW), North-East (NE), South-West (SW), and South-East (SE). Each installation consists of 10 temperature sensors, of which seven are used to measure air temperature at different heights and the remaining three are attached to the several floors using thermal grease for measurement of concrete temperature. Further, the water temperature at inlet and outlet of the FCUs is measured via the temperature sensors $T_{fcu,i}$ and $T_{fcu,o}$ as well as the total flow in the LC, and $n_{lts} = 2$ temperature sensors $T_{lts,k}$, $k = 1, \dots, n_{lts}$ are inserted into thermometer pockets at the top and the bottom of the LTS.

2.4 | Operation conditions and system boundaries

Water circuit temperatures should not exceed $T_{w,max} = 95^\circ\text{C}$ or go below $T_{w,min} = 5^\circ\text{C}$. Temperatures in the PSC should not exceed 110°C to prevent the solar liquid from boiling and changing to a gaseous state, since this would result in a shutdown of the system until all medium has returned to a liquid state, which can typically not be ensured before the upcoming day. To include a certain tolerance region, we therefore define that the temperature of the solar liquid should not exceed $T_{sl,max} = 98^\circ\text{C}$. As a further safety measure, P_{psc} must be in full operation as soon as one solar collector array temperature exceeds $T_{sc,so} = 65^\circ\text{C}$.

Operation of the ACM in FC mode is allowed only at ambient temperatures $T_{amb} \geq 4^\circ\text{C}$. For operation in AC mode, the temperature of the water entering the HT side of the machine must not exceed $T_{ac,ht,max} = 95^\circ\text{C}$ and should not go below $T_{ac,ht,min} = 55^\circ\text{C}$, the temperature of the water entering the LT side of the ACM must not go below $T_{ac,lt,min} = 10^\circ\text{C}$, and the ACM should only be active at ambient temperatures above $T_{ac,amb,min} = 15^\circ\text{C}$ and below $T_{ac,amb,max} = 38^\circ\text{C}$. Further, minimum operation times of 60 minutes for the AC mode and 15 min for the FC mode are defined.

[†]In winter operation, the FCUs are supported by medium from the HTS, which is determined by a switching valve in the LC.

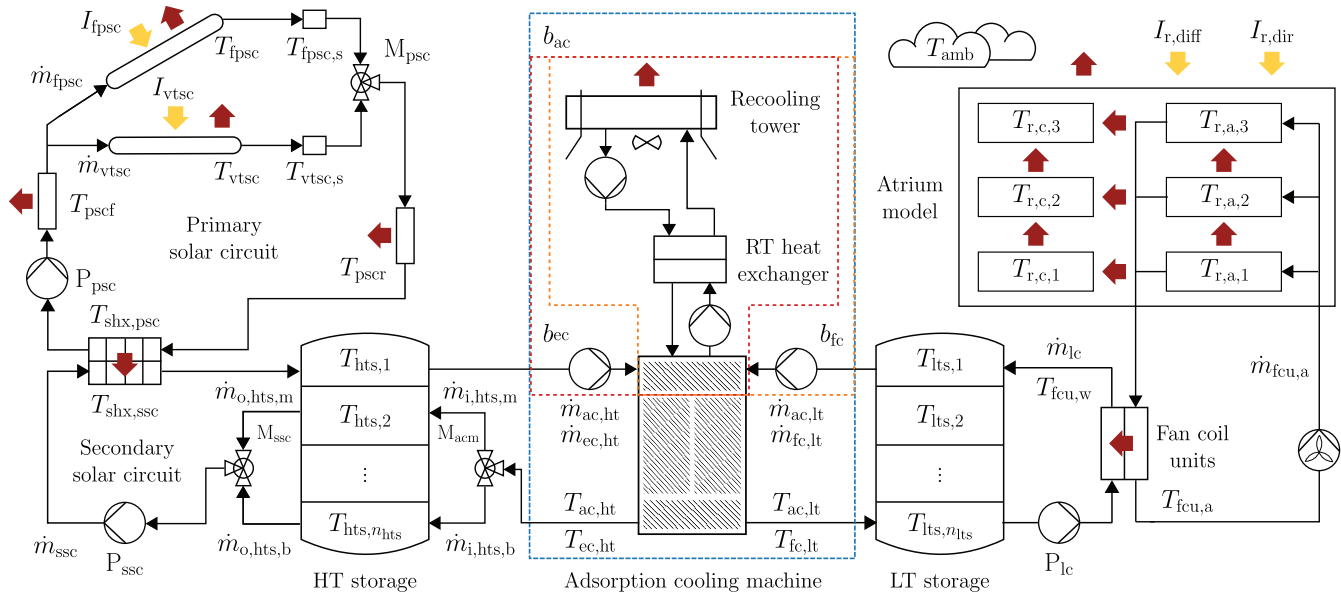


FIGURE 4 Schematic depiction of the solar thermal climate system model

2.5 | Programmable logic controller

The control signals are sent to the several components using a programmable logic controller (PLC). This controller can operate the system either using a conventional, proportional-integral-derivative (PID) and set-point-based control scheme that is implemented directly on the PLC itself, or it can operate the system using external control signals that the controller receives via a network interface.

Independently from the currently used control strategy, the PLC monitors the system temperatures and detects violations of previously specified safety limits. In such a case, the PLC automatically takes over control of the system, and aims to rapidly restore valid operation conditions. For example, in case the temperatures in the PSC exceed 108°C , the EC mode of the ACM is automatically activated.

3 | CONTROL-ORIENTED MODELING OF THE SOLAR THERMAL CLIMATE SYSTEM

The system is modeled using nonlinear grey-box models based on mass and energy balances, resulting in a system of explicit ordinary differential equations (ODEs). The model fulfills all necessary conditions regarding differentiability for later application within derivative-based optimization methods.³⁴ Material and media are assumed to be incompressible and with constant material properties. A schematic depiction of the system model is given in Figure 4. Model parameters are either taken from manufacturer data sheets, if possible, or are the results of system identification and parameter estimation procedures based on measurement data. In the following, component- and circuit-models are described in more detail and information on the corresponding system identification processes is given.

3.1 | Mass flows, pumps, and mixing valves

For simplicity, we do not model pumps and mixing valves explicitly, but assume that the mass flows in the circuits of the system can be controlled directly and on a continuous scale starting from zero. For this to be applicable, a priori measurements from the physical system that determine the volume flows resulting from different pump speeds and mixing valve positions have been obtained.

For pump modeling, we also neglect their minimal part load behavior. Therefore, it must be ensured that if the controller requests a mass flow rate below the minimal rate that a pump can produce, the amount of mass transport resulting

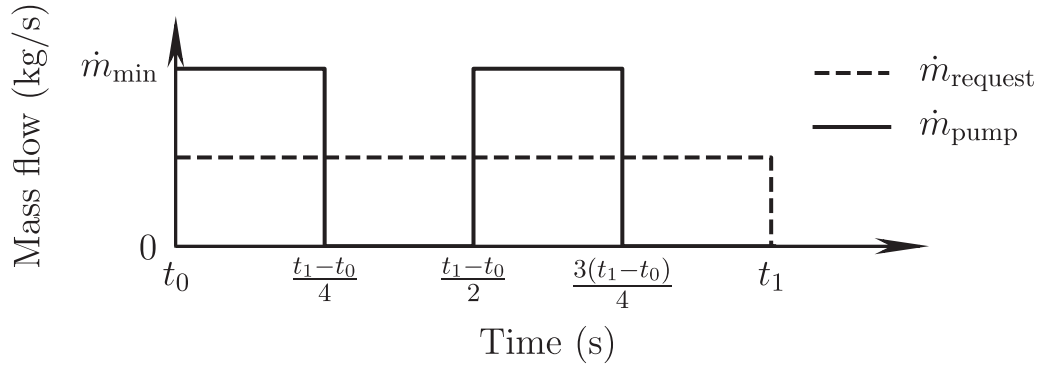


FIGURE 5 Exemplary depiction of mass flow pulsing: in the depiction, \dot{m}_{request} is the mass flow requested by the controller for the time interval $[t_0, t_1]$, which is smaller than the minimum mass flow \dot{m}_{min} that the concerned pump can produce. Therefore, the pump is operated several times at its minimum flow rate during the interval, such that $\int_{t_0}^{t_1} \dot{m}_{\text{pump}}(t) dt = \int_{t_0}^{t_1} \dot{m}_{\text{request}}(t) dt$

from the request over a certain period of time is realized for the physical system by pulsing at minimal flow rate, cf. Figure 5.[‡]

For the pump P_{ssc} , measurements indicate an almost linear correlation between the pump speed v_{pssc} and the mass flow \dot{m}_{ssc} in the SSC. The same holds for the speed v_{plc} of the pump P_{lc} and the mass flow \dot{m}_{lc} in the LC. Therefore, with $\dot{m}_{\text{ssc},\text{max}} = 0.625 \frac{\text{kg}}{\text{s}}$, $\dot{m}_{\text{lc},\text{max}} = 0.5 \frac{\text{kg}}{\text{s}}$, and $v_{\text{pssc}}, v_{\text{plc}} \in [0, 1]$, the corresponding mass flows are determined as

$$\dot{m}_{\text{ssc}}(t) = \dot{m}_{\text{ssc},\text{max}} v_{\text{pssc}}(t), \quad (1)$$

$$\dot{m}_{\text{lc}}(t) = \dot{m}_{\text{lc},\text{max}} v_{\text{plc}}(t). \quad (2)$$

For modeling the effect of the mixing valve M_{ssc} , we assume that the flow separation between outlets $O_{\text{hts},\text{m}}$ and $O_{\text{hts},\text{b}}$ depends linearly on the position $p_{\text{mssc}} \in [0, 1]$, so that the mass flows through $O_{\text{hts},\text{m}}$ and $O_{\text{hts},\text{b}}$ are given by

$$\dot{m}_{\text{o,hts},\text{m}}(t) = p_{\text{mssc}}(t) \dot{m}_{\text{ssc}}(t), \quad (3)$$

$$\dot{m}_{\text{o,hts},\text{b}}(t) = (1.0 - p_{\text{mssc}}(t)) \dot{m}_{\text{ssc}}(t). \quad (4)$$

However, to avoid the increase of model nonlinearity introduced by the multiplication of two control variables, we introduce the mass flow $\dot{m}_{\text{o,hts},\text{b}}$ through $O_{\text{hts},\text{b}}$ as an individual optimization variable instead of p_{mssc} , and formulate accordingly

$$\dot{m}_{\text{o,hts},\text{m}}(t) = \dot{m}_{\text{ssc}}(t) - \dot{m}_{\text{o,hts},\text{b}}(t). \quad (5)$$

Variable $\dot{m}_{\text{o,hts},\text{b}}$ enters the model as a state of the system as

$$\frac{d\dot{m}_{\text{o,hts},\text{b}}(t)}{dt} = \Delta \dot{m}_{\text{o,hts},\text{b}}(t) \quad (6)$$

and the change of the mass flow rate $\Delta \dot{m}_{\text{o,hts},\text{b}}$ as a control variable. Since $\dot{m}_{\text{o,hts},\text{b}}$ is introduced as a substitute for the mixing valve position p_{mssc} , this formulation facilitates to penalize position changes for M_{ssc} via inclusion of $\Delta \dot{m}_{\text{o,hts},\text{b}}$ in the mixed-integer optimal control problem (MIOCP) objective, and with this, to avoid frequent opening and closing of the valve. Analogously, for inlets $I_{\text{hts},\text{m}}$ and $I_{\text{hts},\text{b}}$ and their mass flows $\dot{m}_{\text{i,hts},\text{m}}$ and $\dot{m}_{\text{i,hts},\text{b}}$ with

[‡]This approach becomes applicable due to the assumption that the pumps are typically operated at higher speeds and their comparatively short startup time of approximately 1–2 s, and is therefore not suitable for modeling of the switching behavior of the ACM.

$$\dot{m}_{i,hts,m}(t) = p_{macm}(t)b_{ac}(t)\dot{m}_{ac,ht}, \quad (7)$$

$$\dot{m}_{i,hts,b}(t) = (1.0 - p_{macm}(t))b_{ac}(t)\dot{m}_{ac,ht}, \quad (8)$$

and $p_{macm} \in [0, 1]$, we introduce $\dot{m}_{i,hts,b}$ as an individual optimization variable, and formulate accordingly

$$\dot{m}_{i,hts,m}(t) = b_{ac}(t)\dot{m}_{ac,ht} - \dot{m}_{i,hts,b}(t), \quad (9)$$

while the HT side mass flow induced by the ACM is constant at $\dot{m}_{ac,ht} = 0.69 \frac{\text{kg}}{\text{s}}$ when the machine is operating in AC mode. Variable $\dot{m}_{i,hts,b}$ also enters the model as a state of the system as

$$\frac{d\dot{m}_{i,hts,b}(t)}{dt} = \Delta\dot{m}_{i,hts,b}(t) \quad (10)$$

and the change of the mass flow rate $\Delta\dot{m}_{i,hts,b}$ as a control variable. The corresponding mixing valve positions for the PLC to set are determined from the ratios of the requested mass flows.

The flow sensor installed in the PSC solely measures the total flow in the circuit but not in the individual collector arrays. Therefore, the flow in each array depending on P_{psc} and M_{psc} was determined for different speeds v_{ppsc} and valve positions p_{mpsc} from the individual array outlet temperatures, the total flow, and the temperature resulting from mixing of both flows at the outlet of M_{psc} . Since the individual flows can only be identified from their mixing temperature when the temperature difference between flows is sufficiently high, one collector array was covered using tarpaulins during the measurement process. Afterward, the process was repeated with the other array covered. Since density and viscosity of the solar liquid are influenced by its current temperature but not explicitly considered, the identification was carried out with liquid temperatures above 40 °C so that the identified flows match the real occurring flows better at higher temperature, which is the desired operation state and where inaccuracies are assumed to be more critical.

The resulting flows are depicted in Figure 6 and show a highly nonlinear correlation. To depict these correlations in a suitable way and respecting the necessity for differentiability of the model, suitable B-spline interpolation functions³⁵ $\iota_{vtsc}(\cdot)$ and $\iota_{fpvc}(\cdot)$ are used to depict the individual mass flows \dot{m}_{vtsc} and \dot{m}_{fpvc} as

$$\dot{m}_{vtsc}(t) = \iota_{vtsc}(v_{ppsc}(t), p_{mpsc}(t)), \quad (11)$$

$$\dot{m}_{fpvc}(t) = \iota_{fpvc}(v_{ppsc}(t), p_{mpsc}(t)). \quad (12)$$

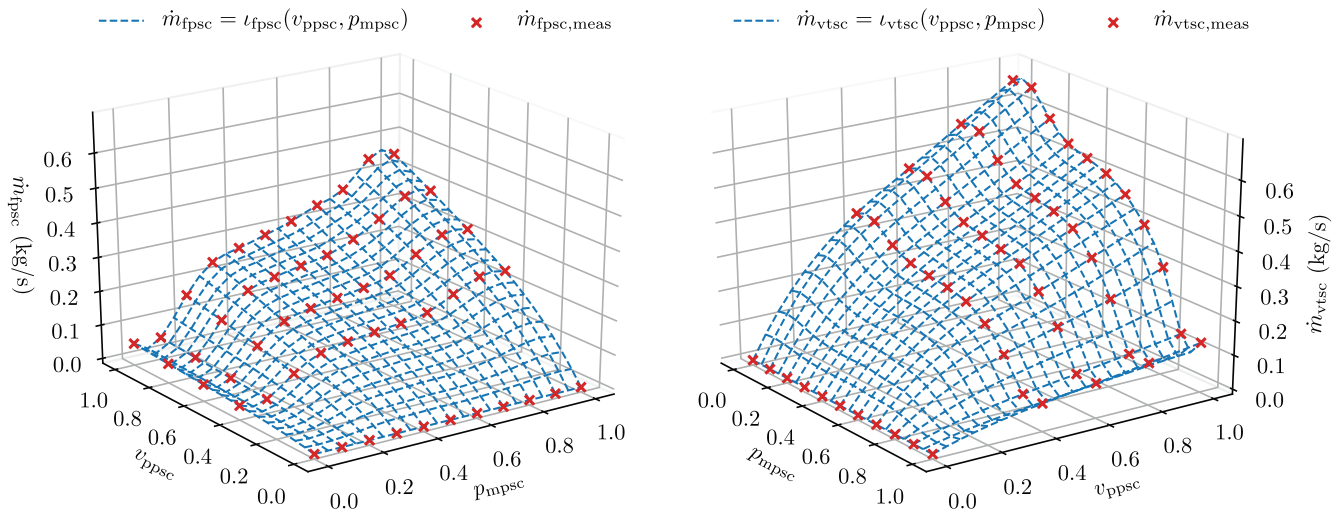


FIGURE 6 Comparison of measured mass flows in the collector arrays depending on pump speed v_{ppsc} and mixing valve position p_{mpsc} to the results of B-spline interpolation

The valve position p_{mpsc} is considered as a state of the system with

$$\frac{dp_{\text{mpsc}}(t)}{dt} = \Delta p_{\text{mpsc}}(t) \quad (13)$$

and the change of the position Δp_{mpsc} as a control variable.

3.2 | Influence of external factors

The system is influenced by external factors, which we distinguish between ambient conditions and indoor conditions. Since no facilities for measurement or forecasting of indoor conditions such as building usage and occupancy are available, indoor conditions are in the following considered as noise acting on the system which is estimated during operation.

As ambient conditions, we regard the ambient temperature T_{amb} and several quantities of solar irradiation. More precisely, we consider the total radiation on the VTSC I_{vtsc} and on the FPSC I_{fpsc} as well as the direct irradiation $I_{\text{r,dir}}$ and diffuse irradiation $I_{\text{r,diff}}$ acting on the building, which are adapted according to the geometrical properties of their corresponding model components. For these quantities, forecast data can be obtained.

Since the quality of the utilized forecasts highly influences the overall MPC performance, forecast data should be adapted based on current measurements of the corresponding quantities. For this, additional states which in the following are entitled as *auxiliary states* are introduced to the model, whose values are estimated during system operation. Exemplified on the ambient temperature, the term T_{amb} used within modeling of the system is

$$T_{\text{amb}}(t) = T_{\text{amb,fc}}(t) - \Delta T_{\text{amb}}(t), \quad (14)$$

where $T_{\text{amb,fc}}$ is the forecast of the ambient temperature and ΔT_{amb} is the auxiliary state to compensate the difference between the forecast and its currently measured value. The development of ΔT_{amb} is described by

$$\frac{d\Delta T_{\text{amb}}(t)}{dt} = -\frac{\Delta T_{\text{amb}}(t)}{\tau_{\Delta T_{\text{amb}}}} + w_{\Delta T_{\text{amb}}}(t), \quad (15)$$

with $\tau_{\Delta T_{\text{amb}}}$ an adequate time constant, which results in a decaying influence of the current measurement on future time points. The term $w_{\Delta T_{\text{amb}}}$ is an additive white process noise term which is used within MHE and considered zero within MPC.

3.3 | High-temperature storage

The HTS is discretized into $n_{\text{hts}} = 4$ volumes with a water mass $m_{\text{hts}} = \rho_w V_{\text{hts}}/n_{\text{hts}}$ each, where ρ_w is the density of water, to depict the temperature distribution in the stratified HTS, cf. Reference 36. The number of layers has been determined by a trial-and-error approach, where $n_{\text{hts}} = 4$ showed sufficient quality while still incorporating only a reasonable amount of states.

The direction and magnitude of mass flows in between those layers depend on their position along the storage height and the current machinery operation. While in simulation models and software alternating mass flows are typically depicted using min/max- or if/else-clauses, these introduce discontinuities to a model and must be avoided to preserve differentiability. Therefore, we formulate the energy balances for the HTS in a differentiable form by following an approach presented by Reference 37.

Under the assumption that inlet $I_{\text{hts,t}}$ and outlet $O_{\text{hts,t}}$ only interact with the top layer of the HTS, we formulate the energy balance that determines the temperature $T_{\text{hts,1}}$ of the top layer of the HTS as

$$\begin{aligned} \frac{dT_{\text{hts,1}}(t)}{dt} = & \frac{1}{m_{\text{hts}}} (\dot{m}_{\text{ssc}}(t) T_{\text{shx,ssc},n_{\text{shx}}}(t) - b_{\text{ac}}(t) \dot{m}_{\text{ac,ht}} T_{\text{hts,1}}(t) - \dot{m}_{\text{hts,t,s}}(t) \frac{T_{\text{hts,1}}(t) + T_{\text{hts,2}}(t)}{2} \\ & - \dot{m}_{\text{hts,t,s}}(t) \frac{T_{\text{hts,1}}(t) - T_{\text{hts,2}}(t)}{2} - \frac{\lambda_{\text{hts,1}}}{c_w} (T_{\text{hts,1}}(t) - T_{\text{amb}}(t))), \end{aligned} \quad (16)$$

$$\dot{m}_{\text{hts},t,s}(t) = \dot{m}_{\text{ssc}}(t) - b_{\text{ac}}(t)\dot{m}_{\text{ac},\text{ht}}, \quad (17)$$

$$\dot{m}_{\text{hts},t,\bar{s}}(t) = \sqrt{\dot{m}_{\text{hts},t,s}(t)^2 + \epsilon_{\text{hts}}}, \quad (18)$$

with c_w the specific heat capacity of water, λ_{hts} the thermal conductance for the heat loss of the HTS to its ambient[§] identified from storage temperature measurements, and $\dot{m}_{\text{hts},t,s}$ the sum of the mass flows entering and leaving the top layer. Variable $\dot{m}_{\text{hts},t,\bar{s}}$ is a smooth approximation for the absolute value of $\dot{m}_{\text{hts},t,s}$, which is better the smaller ϵ_{hts} is chosen. However, smaller values for ϵ_{hts} result in increased nonlinearity of the model, which renders ϵ_{hts} a tuning parameter to be chosen based on the actual quantities of the involved mass flows and the desired accuracy of the approximation. In the following, we use $\epsilon_{\text{hts}} = 10^{-2}$. The state $T_{\text{shx,ssc},n_{\text{shx}}}$ is the temperature state at the outlet of the SSC-side of the SHX model, which is described in more detail later in this section.

The bottom layer of the HTS contains the inlet $I_{\text{hts},b}$ and outlet $O_{\text{hts},b}$ and the energy balance that determines its temperature $T_{\text{hts},n_{\text{hts}}}$ is given by

$$\begin{aligned} \frac{dT_{\text{hts},n_{\text{hts}}}(t)}{dt} = & \frac{1}{m_{\text{hts}}} (\dot{m}_{i,\text{hts},b}(t)T_{\text{ac},\text{ht}}(t) - \dot{m}_{o,\text{hts},b}(t)T_{\text{hts},n_{\text{hts}}}(t) - \dot{m}_{\text{hts},b,s}(t) \frac{T_{\text{hts},n_{\text{hts}}}(t) + T_{\text{hts},n_{\text{hts}}-1}(t)}{2} \\ & - \dot{m}_{\text{hts},b,\bar{s}}(t) \frac{T_{\text{hts},n_{\text{hts}}}(t) - T_{\text{hts},n_{\text{hts}}-1}(t)}{2} - \frac{\lambda_{\text{hts},n_{\text{hts}}}}{c_w} (T_{\text{hts},n_{\text{hts}}}(t) - T_{\text{amb}}(t))), \end{aligned} \quad (19)$$

$$\dot{m}_{\text{hts},b,s}(t) = \dot{m}_{i,\text{hts},b}(t) - \dot{m}_{o,\text{hts},b}(t), \quad (20)$$

$$\dot{m}_{\text{hts},b,\bar{s}}(t) = \sqrt{\dot{m}_{\text{hts},b,s}(t)^2 + \epsilon_{\text{hts}}}, \quad (21)$$

with $T_{\text{ac},\text{ht}}$ the outlet temperatures on the HT side of the ACM in AC mode, $\dot{m}_{\text{hts},b,s}$ the sum of the mass flows entering and leaving the bottom layer, and $\dot{m}_{\text{hts},b,\bar{s}}$ a smooth approximation for the absolute value of $\dot{m}_{\text{hts},b,s}$.

The HTS layer 3 is assumed to interact only with its neighboring layers 2 and n_{hts} , so that its energy balance is given by

$$\begin{aligned} \frac{dT_{\text{hts},3}(t)}{dt} = & \frac{1}{m_{\text{hts}}} (-\dot{m}_{\text{hts},b,\bar{s}}(t)T_{\text{hts},3}(t) + \dot{m}_{\text{hts},b,s}(t) \frac{T_{\text{hts},n_{\text{hts}}}(t) - T_{\text{hts},2}(t)}{2} + \dot{m}_{\text{hts},b,\bar{s}}(t) \frac{T_{\text{hts},n_{\text{hts}}}(t) + T_{\text{hts},2}(t)}{2} \\ & - \frac{\lambda_{\text{hts},3}}{c_w} (T_{\text{hts},3}(t) - T_{\text{amb}}(t))). \end{aligned} \quad (22)$$

Finally, layer 2 of the HTS is assumed to interact with inlet $I_{\text{hts},m}$ and outlet $O_{\text{hts},m}$ in addition to its neighboring layers, so that the energy balance that determines the temperature $T_{\text{hts},2}$ of this layer reads as

$$\begin{aligned} \frac{dT_{\text{hts},2}(t)}{dt} = & \frac{1}{m_{\text{hts}}} ((b_{\text{ac}}(t)\dot{m}_{\text{ac},\text{ht}} - \dot{m}_{i,\text{hts},b}(t))T_{\text{ac},\text{ht}}(t) - (\dot{m}_{\text{ssc}}(t) - \dot{m}_{o,\text{hts},b}(t))T_{\text{hts},2}(t) \\ & + \dot{m}_{\text{hts},t,s}(t) \frac{T_{\text{hts},1}(t) + T_{\text{hts},2}(t)}{2} + \dot{m}_{\text{hts},t,\bar{s}}(t) \frac{T_{\text{hts},1}(t) - T_{\text{hts},2}(t)}{2} \\ & + \dot{m}_{\text{hts},b,s}(t) \frac{T_{\text{hts},3}(t) + T_{\text{hts},2}(t)}{2} + \dot{m}_{\text{hts},b,\bar{s}}(t) \frac{T_{\text{hts},3}(t) - T_{\text{hts},2}(t)}{2} \\ & - \frac{\lambda_{\text{hts},2}}{c_w} (T_{\text{hts},2}(t) - T_{\text{amb}}(t))). \end{aligned} \quad (23)$$

3.4 | Solar circuits

For modeling of the solar collector arrays, system identification showed that the use of one state per array already provides sufficient quality in depiction of the collector temperatures. Therefore, the temperatures T_{vtsc} and T_{fpsc} of the VTSC and FPSC, respectively, are determined by

[§]The HTS is located in a cellar room of the building whose temperature is influenced by the ambient. Since forecasts for the exact room temperature are not available, current heat losses of an HTS layer to its surrounding are approximated via a relation to the current ambient temperature.

$$\frac{dT_{vtsc}(t)}{dt} = \frac{1}{C_{vtsc}} (\dot{m}_{vtsc}(t)c_{sl}(T_{psc}(t) - T_{vtsc}(t)) + \eta_{vtsc}A_{vtsc}I_{vtsc}(t) - (\alpha_{vtsc} + \Delta_{\alpha_{vtsc}}(t))A_{vtsc}(T_{vtsc}(t) - T_{amb}(t))), \quad (24)$$

$$\frac{dT_{fpvc}(t)}{dt} = \frac{1}{C_{fpvc}} (\dot{m}_{fpvc}(t)c_{sl}(T_{psc}(t) - T_{fpvc}(t)) + \eta_{fpvc}A_{fpvc}I_{fpvc}(t) - (\alpha_{fpvc} + \Delta_{\alpha_{fpvc}}(t))A_{fpvc}(T_{fpvc}(t) - T_{amb}(t))), \quad (25)$$

with C_{vtsc} , C_{fpvc} the heat capacities of each collector array including the contained medium, η_{vtsc} , η_{fpvc} their optical efficiencies, and α_{vtsc} , α_{fpvc} the heat transfer coefficients for the heat losses to the ambient of each array.³⁸ For consideration of unmodeled influences on collector heat losses induced by, for example, wind, the auxiliary states $\Delta_{\alpha_{vtsc}}$ and $\Delta_{\alpha_{fpvc}}$ are introduced, whose values are estimated during system operation and whose development is described by

$$\frac{d\Delta_{\alpha_{vtsc}}(t)}{dt} = w_{\Delta_{\alpha_{vtsc}}}(t), \quad (26)$$

$$\frac{d\Delta_{\alpha_{fpvc}}(t)}{dt} = w_{\Delta_{\alpha_{fpvc}}}(t), \quad (27)$$

with $w_{\Delta_{\alpha_{vtsc}}}$ and $w_{\Delta_{\alpha_{fpvc}}}$ additive white process noise terms used within MHE and considered zero within MPC.

As described in Section 2, the temperature of the collector arrays cannot be measured directly, but only via the sensors T_{vtsc} and T_{fpvc} . Their temperatures $T_{vtsc,s}$ and $T_{fpvc,s}$ are determined by energy balances over a short piece of the PSC pipe as

$$\frac{dT_{vtsc,s}(t)}{dt} = \frac{1}{V_{vtsc,s}\rho_{sl}c_{sl}} (\dot{m}_{vtsc}(t)c_{sl}(T_{vtsc}(t) - T_{vtsc,s}(t)) - \lambda_{vtsc,s}(T_{vtsc,s}(t) - T_{amb}(t))), \quad (28)$$

$$\frac{dT_{fpvc,s}(t)}{dt} = \frac{1}{V_{fpvc,s}\rho_{sl}c_{sl}} (\dot{m}_{fpvc}(t)c_{sl}(T_{fpvc}(t) - T_{fpvc,s}(t)) - \lambda_{fpvc,s}(T_{fpvc,s}(t) - T_{amb}(t))), \quad (29)$$

with $V_{vtsc,s}$, $V_{fpvc,s}$ the pipe volumes for the sensors, $\lambda_{vtsc,s}$, $\lambda_{fpvc,s}$ their thermal conductances for the heat losses to the ambient, and c_{sl} and ρ_{sl} the specific heat capacity and density of the solar liquid, respectively.

Since the amount of liquid in the PSC is rather large, the mass transport from the roof to the cellar introduces a delayed availability of the heat collected by the solar arrays. This behavior is modeled using two energy balances that depict the temperature of the medium in the feed line pipe T_{psc} and the return line pipe T_{pscr} , respectively, as follows

$$\frac{dT_{psc}(t)}{dt} = \frac{1}{C_{psc}} ((\dot{m}_{vtsc}(t) + \dot{m}_{fpvc}(t))c_{sl}(T_{shx,psc,n_{shx}}(t) - T_{psc}(t)) - \lambda_{psc}(T_{psc}(t) - T_{amb}(t))), \quad (30)$$

$$\frac{dT_{pscr}(t)}{dt} = \frac{1}{C_{pscr}} (\dot{m}_{vtsc}(t)c_{sl}T_{vtsc,s}(t) + \dot{m}_{fpvc}(t)c_{sl}T_{fpvc,s}(t) - (\dot{m}_{vtsc}(t) + \dot{m}_{fpvc}(t))c_{sl}T_{pscr}(t) - \lambda_{pscr}(T_{pscr}(t) - T_{amb}(t))), \quad (31)$$

with C_{psc} the heat capacity of one pipe including the contained medium, λ_{psc} the thermal conductance for the heat losses of one pipe to the ambient, and $T_{shx,psc,n_{shx}}$ the temperature state at the outlet of the PSC-side of the SHX model.

The model for the SHX consists of $n_{shx} = 4$ energy balances per side of the SHX where opposing volumes exchange heat depending on a heat transfer coefficient α_{shx} and heat exchange area A_{shx} . The temperature states $T_{shx,psc,1}$ and $T_{shx,ssc,1}$ at the inlets of each side of the SHX are determined by

$$\begin{aligned} \frac{dT_{shx,psc,1}(t)}{dt} &= \frac{n_{shx}}{V_{shx}\rho_{sl}c_{sl}} ((\dot{m}_{vtsc}(t) + \dot{m}_{fpvc}(t))c_{sl}(T_{pscr}(t) - T_{shx,psc,1}(t)) \\ &\quad - \frac{A_{shx}}{n_{shx}}\alpha_{shx}(T_{shx,psc,1}(t) - T_{shx,ssc,n_{shx}}(t))), \end{aligned} \quad (32)$$

$$\begin{aligned} \frac{dT_{shx,ssc,1}(t)}{dt} &= \frac{n_{shx}}{V_{shx}\rho_w c_w} ((\dot{m}_{ssc}(t) - \dot{m}_{o,hts,b}(t))c_w T_{hts,2}(t) + \dot{m}_{o,hts,b}(t)c_w T_{hts,n_{hts}}(t) - \dot{m}_{ssc}(t)c_w T_{shx,ssc,1}(t) \\ &\quad + \frac{A_{shx}}{n_{shx}}\alpha_{shx}(T_{shx,psc,n_{shx}}(t) - T_{shx,ssc,1}(t))), \end{aligned} \quad (33)$$

and the remaining temperature states per side of the SHX are determined by

$$\frac{dT_{\text{shx,psc},k}(t)}{dt} = \frac{n_{\text{shx}}}{V_{\text{shx}}\rho_{\text{sl}}c_{\text{sl}}}((\dot{m}_{\text{vtsc}}(t) + \dot{m}_{\text{fpse}}(t))c_{\text{sl}}(T_{\text{shx,psc},k-1}(t) - T_{\text{shx,psc},k}(t)) - \frac{A_{\text{shx}}}{n_{\text{shx}}}\alpha_{\text{shx}}(T_{\text{shx,psc},k}(t) - T_{\text{shx,ssc},(n_{\text{shx}}+1-k)}(t))), \quad k = 2, \dots, n_{\text{shx}}, \quad (34)$$

$$\frac{dT_{\text{shx,ssc},k}(t)}{dt} = \frac{n_{\text{shx}}}{V_{\text{shx}}\rho_{\text{w}}c_{\text{w}}}(\dot{m}_{\text{ssc}}(t)c_{\text{w}}(T_{\text{shx,ssc},k-1}(t) - T_{\text{shx,ssc},k}(t)) + \frac{A_{\text{shx}}}{n_{\text{shx}}}\alpha_{\text{shx}}(T_{\text{shx,psc},(n_{\text{shx}}+1-k)}(t) - T_{\text{shx,ssc},k}(t))), \quad k = 2, \dots, n_{\text{shx}}. \quad (35)$$

3.5 | Cooling machine

The ACM is a static model describing the relations between inlet and outlet temperatures of the machine's circuits in its different operation modes, which in turn influence the temperatures of the HTS and LTS once a mode is active.

While only the AC mode utilizes the ACM itself, the FC and EC modes only utilize the RTHX. Measurements at the physical system have shown that the LT outlet temperatures of the ACM in FC mode can be sufficiently depicted by a simple temperature difference to the current ambient temperature as

$$T_{\text{fc,lt}}(t) = T_{\text{amb}}(t) + \Delta T_{\text{fc,lt}}. \quad (36)$$

The cooling power $\dot{Q}_{\text{ac,lt}}$ and COP of the machine COP_{ac} in AC mode depend on the inlet temperatures of all three circuits. For the machine used in this study, $\dot{Q}_{\text{ac,lt}}$ and COP_{ac} data can be obtained from the data sheet provided by the manufacturer as averaged values over one complete cycle of the machine and for different combinations of inlet temperatures.

For the ACM model, the temperatures $T_{\text{hts},1}$ and $T_{\text{lts},1}$ are regarded as inlet temperatures of the HT and LT side, respectively. For the temperature at the medium temperature (MT) inlet, we assume that the RT returns medium at a constant difference to the ambient temperature analogously to the FC mode. Therefore, $\dot{Q}_{\text{ac,lt}}$ and COP_{ac} can be determined by^{30,37}

$$\dot{Q}_{\text{ac,lt}}(t) = \iota_{\dot{Q}_{\text{ac,lt}}}(T_{\text{hts},1}(t), T_{\text{lts},1}(t), T_{\text{amb}}(t)), \quad (37)$$

$$\text{COP}_{\text{ac}}(t) = \iota_{\text{COP}_{\text{ac}}}(T_{\text{hts},1}(t), T_{\text{lts},1}(t), T_{\text{amb}}(t)), \quad (38)$$

with $\iota_{\dot{Q}_{\text{ac,lt}}}(\cdot)$ and $\iota_{\text{COP}_{\text{ac}}}(\cdot)$ suitable polynomial fittings to machine data. Using these, the temperatures $T_{\text{ac,ht}}$ and $T_{\text{ac,lt}}$ at the HT and LT outlet of the ACM can be calculated as

$$T_{\text{ac,lt}}(t) = T_{\text{lts},1}(t) - \frac{1}{c_{\text{w}}\dot{m}_{\text{ac,lt}}}\dot{Q}_{\text{ac,lt}}(t), \quad (39)$$

$$T_{\text{ac,ht}}(t) = T_{\text{hts},1}(t) - \frac{1}{c_{\text{w}}\dot{m}_{\text{ac,ht}}}\frac{\dot{Q}_{\text{ac,lt}}(t)}{\text{COP}_{\text{ac}}(t)}. \quad (40)$$

Both the AC mode and FC mode of the ACM are subject to startup and shutdown phases which can take several minutes to complete, while the phases of the FC mode typically take less time to finish than the AC mode phases. Since these phases are not considered in the developed model, frequent switching of modes, especially from and to the AC mode, must be avoided.

As the EC mode of the machine is considered more as a safety measure than a desirable operation mode, active consideration of this mode within MPC is neglected. However, the mode can still be activated by the PLC in case of violations of temperature safety limits.

3.6 | Low-temperature storage and fan coil units

System identification showed that the LTS can be depicted by $n_{\text{LTS}} = 2$ volumes with water mass $m_{\text{LTS}} = \rho_w V_{\text{LTS}} / n_{\text{LTS}}$ to depict the temperature distribution in the stratified LTS. Due to the circumstance that $\dot{m}_{\text{lc,max}} < \dot{m}_{\text{fc,lt}}$ and $\dot{m}_{\text{lc,max}} < \dot{m}_{\text{ac,lt}}$ with $\dot{m}_{\text{fc,lt}} = \dot{m}_{\text{ac,lt}} = 0.8 \frac{\text{kg}}{\text{s}}$, the direction of mass flows inside the LTS is directly determined by whether the ACM is currently operating or not. Therefore, the temperatures of the upper layer $T_{\text{LTS},1}$ and the bottom layer $T_{\text{LTS},n_{\text{LTS}}}$ are determined by the energy balances

$$\begin{aligned} \frac{dT_{\text{LTS},1}(t)}{dt} = & \frac{1}{m_{\text{LTS}}} (\dot{m}_{\text{lc}}(t) T_{\text{fcu,w}}(t) - (1 - b_{\text{ac}}(t) - b_{\text{fc}}(t)) \dot{m}_{\text{lc}}(t) T_{\text{LTS},1}(t) \\ & + b_{\text{ac}}(t) (\dot{m}_{\text{ac,lt}} - \dot{m}_{\text{lc}}(t)) T_{\text{LTS},n_{\text{LTS}}}(t) - b_{\text{ac}}(t) \dot{m}_{\text{ac,lt}} T_{\text{ac,lt}}(t) \\ & + b_{\text{fc}}(t) (\dot{m}_{\text{fc,lt}} - \dot{m}_{\text{lc}}(t)) T_{\text{LTS},n_{\text{LTS}}}(t) - b_{\text{fc}}(t) \dot{m}_{\text{fc,lt}} T_{\text{fc,lt}}(t)), \end{aligned} \quad (41)$$

$$\begin{aligned} \frac{dT_{\text{LTS},n_{\text{LTS}}}(t)}{dt} = & \frac{1}{m_{\text{LTS}}} (-\dot{m}_{\text{lc}}(t) T_{\text{LTS},n_{\text{LTS}}}(t) + (1 - b_{\text{ac}}(t) - b_{\text{fc}}(t)) \dot{m}_{\text{lc}}(t) T_{\text{LTS},1}(t) \\ & - b_{\text{ac}}(t) (\dot{m}_{\text{ac,lt}} - \dot{m}_{\text{lc}}(t)) T_{\text{LTS},n_{\text{LTS}}}(t) + b_{\text{ac}}(t) \dot{m}_{\text{ac,lt}} T_{\text{ac,lt}}(t) \\ & - b_{\text{fc}}(t) (\dot{m}_{\text{fc,lt}} - \dot{m}_{\text{lc}}(t)) T_{\text{LTS},n_{\text{LTS}}}(t) + b_{\text{fc}}(t) \dot{m}_{\text{fc,lt}} T_{\text{fc,lt}}(t)), \end{aligned} \quad (42)$$

with $T_{\text{ac,lt}}$ and $T_{\text{fc,lt}}$ the LT outlet temperatures of the ACM in AC and FC mode, respectively. The temperatures of the water side $T_{\text{fcu,w}}$ and of the air side $T_{\text{fcu,a}}$ of the FCUs are determined by

$$\frac{dT_{\text{fcu,w}}(t)}{dt} = \frac{1}{C_{\text{fcu,w}}} (\dot{m}_{\text{lc}}(t) c_w (T_{\text{LTS},n_{\text{LTS}}}(t) - T_{\text{fcu,w}}(t)) - \dot{Q}_{\text{fcu,r}}(t)), \quad (43)$$

$$\frac{dT_{\text{fcu,a}}(t)}{dt} = \frac{1}{C_{\text{fcu,a}}} (\dot{m}_{\text{fcu,a}} c_a (T_{\text{r,a},1}(t) - T_{\text{fcu,a}}(t)) + \dot{Q}_{\text{fcu,r}}(t)), \quad (44)$$

$$\dot{Q}_{\text{fcu,r}}(t) = \lambda_{\text{fcu}} (T_{\text{fcu,w}}(t) - T_{\text{fcu,a}}(t)), \quad (45)$$

with $C_{\text{fcu,w}}$ and $C_{\text{fcu,a}}$ the thermal capacities of the water and air side of the FCUs, respectively, λ_{fcu} the thermal conductance between those sides, $T_{\text{r,a},1}$ the temperature of the bottom air layer of the room model, and $\dot{Q}_{\text{fcu,r}}$ the total heat exchanged between FCUs and room air. The air mass flow $\dot{m}_{\text{fcu,a}}$ is assumed constant within the model, however, for the physical system the FCUs are only operated if $\dot{m}_{\text{lc}} > 0 \frac{\text{kg}}{\text{s}}$ for saving of energy.

3.7 | Room model

Since the atrium extends over several floors, the model that depicts the room temperature is discretized into $n_r = 3$ layers of air and concrete masses along the room's height with corresponding temperatures $T_{\text{r,a},k}$ and $T_{\text{r,c},k}$, $k = 1, \dots, n_r$. The heat flows acting on these temperatures depend on the ambient temperature T_{amb} , the direct solar irradiation $I_{\text{r,dir}}$ and the diffuse solar irradiation $I_{\text{r,diff}}$ on the building, as well as the heat exchange $\dot{Q}_{\text{fcu,r}}$ with the FCUs. Under these assumptions, a grey-box resistance-capacitance (RC) model has been identified for the atrium within an extensive system identification campaign which reads as

$$\begin{aligned} \frac{dT_{\text{r,a},1}(t)}{dt} = & \frac{1}{C_{\text{r,a}}} \left(-\frac{1}{R_{\text{r,a,c},1}} (T_{\text{r,a},1}(t) - T_{\text{r,c},1}(t)) + \frac{1}{R_{\text{r,a,amb}}} (T_{\text{amb}}(t) - T_{\text{r,a},1}(t)) + \frac{1}{R_{\text{r,a,a}}} (T_{\text{r,a},2}(t) - T_{\text{r,a},1}(t)) \right. \\ & \left. - r_{\text{fcu,r},1} \dot{Q}_{\text{fcu,r}}(t) + r_{\text{i,dir,a},1} I_{\text{r,dir}}(t) + r_{\text{i,diff,a},1} I_{\text{r,diff}}(t) + \dot{Q}_{\text{n,a},1}(t) \right), \end{aligned} \quad (46)$$

$$\begin{aligned} \frac{dT_{\text{r,a},2}(t)}{dt} = & \frac{1}{C_{\text{r,a}}} \left(-\frac{1}{R_{\text{r,a,c},2}} (T_{\text{r,a},2}(t) - T_{\text{r,c},2}(t)) + \frac{1}{R_{\text{r,a,amb}}} (T_{\text{amb}}(t) - T_{\text{r,a},2}(t)) - \frac{1}{R_{\text{r,a,a}}} (T_{\text{r,a},2}(t) - T_{\text{r,a},1}(t)) \right. \\ & \left. + \frac{1}{R_{\text{r,a,a}}} (T_{\text{r,a},n_r}(t) - T_{\text{r,a},2}(t)) - r_{\text{fcu,r},2} \dot{Q}_{\text{fcu,r}}(t) + r_{\text{i,dir,a},2} I_{\text{r,dir}}(t) + r_{\text{i,diff,a},2} I_{\text{r,diff}}(t) + \dot{Q}_{\text{n,a},2}(t) \right), \end{aligned} \quad (47)$$

$$\frac{dT_{r,a,n_r}(t)}{dt} = \frac{1}{C_{r,a}} \left(-\frac{1}{R_{r,a,c,n_r}} (T_{r,a,n_r}(t) - T_{r,c,n_r}(t)) + \frac{1}{R_{r,a,amb}} (T_{amb}(t) - T_{r,a,n_r}(t)) - \frac{1}{R_{r,a,a}} (T_{r,a,n_r}(t) - T_{r,a,2}(t)) \right. \\ \left. - r_{fcu,r,n_r} \dot{Q}_{fcu,r}(t) + r_{i,dir,a,n_r} I_{r,dir}(t) + r_{i,diff,a,n_r} I_{r,diff}(t) + \dot{Q}_{n,a,n_r}(t) \right), \quad (48)$$

$$\frac{dT_{r,c,k}(t)}{dt} = \frac{1}{C_{r,c}} \left(\frac{1}{R_{r,a,c,k}} (T_{r,a,k}(t) - T_{r,c,k}(t)) + \frac{1}{R_{r,c,amb,k}} (T_{amb}(t) - T_{r,c,k}(t)) \right. \\ \left. + r_{i,dir,c,k} I_{r,dir}(t) + r_{i,diff,c,k} I_{r,diff}(t) + \dot{Q}_{n,c,k}(t) \right), \quad k = 1, \dots, n_r. \quad (49)$$

The model identification was carried out in multiple steps. First, a reduced version of the model was identified that contained only the thermal capacities $C_{r,a}$, $C_{r,c}$ and resistances $R_{r,a,amb}$, $R_{r,c,amb}$, $R_{r,a,c,k}$, $k = 1, \dots, n_r$. For this, measurement data obtained during night times at different ambient conditions was utilized, so that the influence of solar irradiation and occupancy on the room temperature was excluded. Also, the FCUs were not operated during that time.

Using the identified capacities and resistances, several ratios $r_{fcu,r,k}$, $k = 1, \dots, n_r$ were introduced to the model that depict the ratio of the total FCU heat exchange $\dot{Q}_{fcu,r}$ for an air mass. Identification of these ratios was carried out using data obtained especially while operating the FCUs during night times.

Afterward, further ratios have been introduced to the model, whereof $r_{i,dir,a,k}$, $r_{i,diff,a,k}$, $k = 1, \dots, n_r$ depict the ratios of the direct and diffuse solar irradiation acting on an air mass and $r_{i,dir,c,k}$, $r_{i,diff,c,k}$, $k = 1, \dots, n_r$ the ratios acting on a concrete mass. These were identified using data obtained during day times especially on weekends and bank holidays to minimize the influence of occupancy on the measured room temperature.

Finally, heat noise terms $\dot{Q}_{n,a,k}$, $\dot{Q}_{n,c,k}$, $k = 1, \dots, n_r$ are introduced to the model to depict unknown influences from, for example, occupancy and air exchange, of which no data are available. Similar to (15), these are regarded as states which are estimated during operation, while their development is described by

$$\frac{d\dot{Q}_{n,a,k}(t)}{dt} = -\frac{\dot{Q}_{n,a,k}(t)}{\tau_{\dot{Q}_{n,a,k}}} + w_{\dot{Q}_{n,a,k}}(t), \quad k = 1, \dots, n_r, \quad (50)$$

$$\frac{d\dot{Q}_{n,c,k}(t)}{dt} = -\frac{\dot{Q}_{n,c,k}(t)}{\tau_{\dot{Q}_{n,c,k}}} + w_{\dot{Q}_{n,c,k}}(t), \quad k = 1, \dots, n_r, \quad (51)$$

with $\tau_{\dot{Q}_{n,a}}$, $\tau_{\dot{Q}_{n,c}}$ adequate time constants and $w_{\dot{Q}_{n,a}}$, $w_{\dot{Q}_{n,c}}$ additive white process noise terms used within MHE and considered zero within MPC.

3.8 | Operation conditions and constraints

For formulation of the operation conditions and constraints, we first introduce a vector s of $n_s = 35$ slack variables with

$$s^T = [\Delta T_{r,a} \ s_{ac,lb}^T \ s_{ac,ub}^T \ s_{ppsc,vpsc} \ s_{ppsc,fpvc} \ s_w^T \ s_{sl}^T]. \quad (52)$$

For control of HVAC systems, it is favorable to define a temperature comfort range instead of tracking a fixed set point temperature, as this provides flexibility for the control algorithm, and with this, further energy saving potential.³⁹ Using the slack variable $\Delta T_{r,a}$ and the room air temperature $T_{r,a,1}$, the deviation of the room air temperature from such a comfort range can be formulated as

$$T_{r,a,min} - \Delta T_{r,a}(t) \leq T_{r,a,1}(t) \leq T_{r,a,max} + \Delta T_{r,a}(t), \quad (53)$$

and using the slack variables $s_{ac,lb}$ and $s_{ac,ub}$, the operation conditions for the AC mode of the ACM stated in Section 2.4 can be formulated as *smoothened vanishing constraints*^{30,40} as

$$b_{ac}(t) \left(\begin{pmatrix} T_{ac,ht,min} - T_{hts,1}(t) \\ T_{ac,lt,min} - T_{lts,1}(t) \\ T_{ac,amb,min} - T_{amb}(t) \end{pmatrix} - s_{ac,lb}(t) \right) \leq \epsilon_{ac,lb}, \quad (54)$$

$$b_{ac}(t) \left(\left(\frac{T_{hts,1}(t) - T_{ac,ht,max}}{T_{amb}(t) - T_{ac,amb,max}} \right) - s_{ac,ub}(t) \right) \leq \epsilon_{ac,ub}, \quad (55)$$

with chosen $\epsilon_{ac,lb} = \epsilon_{ac,ub} = 0.1$ wherein the slack variables can be utilized to relax these constraints if necessary to preserve feasibility when applied within an optimization problem. Further, the constraints

$$(T_{vtsc}(t) - T_{sc,so})(v_{ppsc,so} - s_{ppsc,vtsc}(t)) \leq \epsilon_{sc,so}, \quad (56)$$

$$(T_{fpsc}(t) - T_{sc,so})(v_{ppsc,so} - s_{ppsc,fp}(t)) \leq \epsilon_{sc,so}, \quad (57)$$

$$\begin{pmatrix} s_{ppsc,vtsc}(t) \\ s_{ppsc,fp}(t) \end{pmatrix} - v_{ppsc}(t) \leq 0, \quad (58)$$

with chosen $\epsilon_{sc,so} = 0.1$ implement the safety measure for P_{psc} not to operate below $v_{ppsc,so}$ once one of the collector temperatures exceeds $T_{sc,so}$. Through

$$\dot{m}_{o,hts,b}(t) - \dot{m}_{ssc}(t) \leq 0, \quad \dot{m}_{o,hts,b}(t) \geq 0, \quad (59)$$

$$\dot{m}_{i,hts,b}(t) - b_{ac}(t)\dot{m}_{ac,ht} \leq 0, \quad \dot{m}_{i,hts,b}(t) \geq 0, \quad (60)$$

it is ensured that the mass flow through the several storage outlets and inlets does not exceed the total mass flow induced by the respective pumps. The upper and lower temperature bounds for the water states in x selected by the selection matrix Z_w are defined as *soft constraints*⁴¹ as

$$T_{w,min} - s_w(t) \leq Z_w x(t) \leq T_{w,max} + s_w(t), \quad (61)$$

and the upper bounds for the solar liquid states in the PSC selected by the selection matrix Z_{sl} are defined as

$$Z_{sl} x(t) \leq T_{sl,max} + s_{sl}(t). \quad (62)$$

Different from that, the bounds for state p_{mpsc} are given as hard constraints as in

$$p_{mpsc,min} \leq p_{mpsc}(t) \leq p_{mpsc,max} \quad (63)$$

with $p_{mpsc,min} = 0.1$ and $p_{mpsc,max} = 0.9$, since due to limit switches of the mixing valve, constraint violation here is prevented physically. Finally, an additional upper bound for the temperature state $T_{shx,psc,n_{shx}}$ is introduced as

$$T_{shx,psc,n_{shx}}(t) \leq T_{shx,psc,out,max} + s_{shx,psc,out}(t) \quad (64)$$

with $T_{shx,psc,out,ma} = 85^\circ\text{C}$ and $s_{shx,psc,out} \in s_{sl}$ for further regulation of the temperature of the solar liquid returned from the PSC-side outlet of the SHX to the solar collector array inlets.

3.9 | Model summary

In total, the system consists of $n_x = 42$ states, $n_u = 6$ continuous controls, $n_b = 2$ binary controls, $n_c = 5$ time-varying parameters, $n_y = 22$ measured quantities, and $n_w = 11$ process noise terms, as given by

$$\begin{aligned} x^\top = & [T_{hts,\{1, \dots, n_{hts}\}}, T_{lts,\{1, \dots, n_{lts}\}}, T_{vtsc}, \Delta_{\alpha_{vtsc}}, T_{vtsc,s}, T_{fpsc}, \Delta_{\alpha_{fpsc}}, T_{fpsc,s}, T_{psc}, T_{psc,r}, T_{shx,psc,\{1, \dots, n_{shx}\}}, T_{shx,ssc,\{1, \dots, n_{shx}\}}, \\ & T_{fcu,w}, T_{fcu,a}, T_{r,a,\{1, \dots, n_r\}}, T_{r,c,\{1, \dots, n_r\}}, p_{mpsc}, \dot{m}_{o,hts,b}, \dot{m}_{i,hts,b}, \Delta_{T_{amb}}, \Delta_{I_{vtsc}}, \Delta_{I_{fpsc}}, \dot{Q}_{n,a,\{1, \dots, n_r\}}, \dot{Q}_{n,c,\{1, \dots, n_r\}}], \end{aligned} \quad (65)$$

$$u^\top = [v_{\text{ppsc}}, \Delta p_{\text{mpsc}}, v_{\text{pssc}}, \Delta \dot{m}_{\text{o,hts,b}}, \Delta \dot{m}_{\text{i,hts,b}}, v_{\text{plc}}], \quad (66)$$

$$b^\top = [b_{\text{ac}}, b_{\text{fc}}], \quad (67)$$

$$c^\top = [T_{\text{amb,fc}}, I_{\text{vtsc,fc}}, I_{\text{fpse,fc}}, I_{\text{r,dir,fc}}, I_{\text{r,diff,fc}}], \quad (68)$$

$$w^\top = [w_{\Delta_{T_{\text{amb}}}}, w_{\Delta_{I_{\text{vtsc}}}}, w_{\Delta_{I_{\text{fpse}}}}, w_{\dot{Q}_{\text{n,a}}\{1,\dots,n_r\}}, w_{\dot{Q}_{\text{n,c}}\{1,\dots,n_r\}}, w_{\Delta_{\sigma_{\text{vtsc}}}}, w_{\Delta_{\sigma_{\text{fpse}}}}]. \quad (69)$$

and the system model f consisting of Equations (1), (2), (5), (6), and (9)–(51) is a system of explicit ODEs

$$\frac{dx(t)}{dt} = f_0(x(t), u(t), c(t), w(t)) + \sum_{i=1}^{n_b} b_i(t) \cdot f_i(x(t), u(t), c(t), w(t)) \quad (70)$$

which is directly given in the so-called *partial outer convexified* form, wherein the system dynamics are given as the sum of a function f_0 and the functions $f_i, i=1 \dots, n_b$ whose activity is determined by the corresponding binary controls b_i , of which at most one can be active at a time. Availability of this special structure is important for the solution methods applied in the scope of this work, and can, if not directly given, also be achieved via systematic reformulation, cf. Reference 42.

The system is subject to the constraints (53)–(64) and additional combinatorial constraints regarding the maximum amount of allowed switches and minimum dwell times for the binary controls summarized as

$$h(x(t), u(t), b(\cdot), c(t), s(t)) \leq 0. \quad (71)$$

In (71), the notation $b(\cdot)$ is chosen to indicate that such combinatorial constraints can be coupled over time. The treatment of combinatorial constraints in the scope of this work is explained in more detail later in Section 4.3.

4 | DESCRIPTION AND IMPLEMENTATION OF THE MPC ALGORITHM

In this section, first the MIOCP used within MPC of the system is presented, followed by a description of the algorithm and software used for implementation and solution of the problem. Afterward, the formulation and implementation of the MHE problem utilized within state estimation for the system is presented. The section is concluded by a description of the utilized computational hardware, software, and data sources. The information flow between MPC, MHE, and the plant is illustrated in Figure 7, which shows that the control signals u and b computed by MPC are applied for plant operation, while the measurements y obtained from the plant are used for estimation of the current system state \hat{x} via MHE. For a demo implementation of the presented algorithms with reduced dependencies, we refer the reader to Reference 43.

4.1 | Optimal control problem formulation

With the states x , continuous controls u , binary controls b , time-varying parameters c , and slack variables s introduced in the previous section, the MIOCP reads as

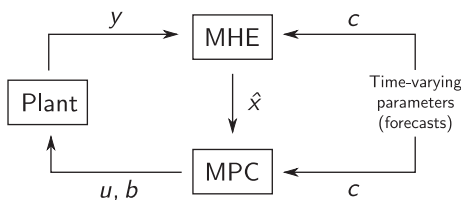


FIGURE 7 Information flow between MPC, MHE, and the plant

$$\begin{aligned} & \text{minimize} \int_{t_0}^{t_f} s(t)^\top W_s s(t) \, dt + \int_{t_0}^{t_f} \omega_s^\top s(t) \, dt + \int_{t_0}^{t_f} u(t)^\top W_u u(t) \, dt + \int_{t_0}^{t_f} \omega_u^\top u(t) \, dt \\ & x(\cdot), u(\cdot), \\ & b(\cdot), s(\cdot) \end{aligned} \quad (72a)$$

subject to for $t \in [t_0, t_f]$:

$$\frac{dx(t)}{dt} = f_0(x(t), u(t), c(t), w(t)) + \sum_{i=1}^{n_b} b_i(t) \cdot f_i(x(t), u(t), c(t), w(t)), \quad (72b)$$

$$h(x(t), u(t), b(\cdot), c(t), s(t)) \leq 0, \quad (72c)$$

$$u_{lb} \leq u(t) \leq u_{ub}, \quad (72d)$$

$$b(t) \in \{0, 1\}^{n_b}, \quad (72e)$$

$$\sum_{i=1}^{n_b} b_i(t) \leq 1, \quad (72f)$$

$$s(t) \geq 0, \quad (72g)$$

$$w(t) = 0, \quad (72h)$$

$$x(t_0) = \hat{x}. \quad (72i)$$

The objective (72a) of the MIOCP is a Lagrange-type economic objective and contains both the sum of squares and the sum of the slack variables s , as well as the sum of squares and the sum of the continuous controls u , weighted by appropriate diagonal weighting matrices $W_s \in \mathbb{R}^{n_s \times n_s}$ and $W_u \in \mathbb{R}^{n_u \times n_u}$ and vectors $\omega_s \in \mathbb{R}^{n_s}$ and $\omega_u \in \mathbb{R}^{n_u}$, respectively.[¶]

The system dynamics described in Section 3 enter the MIOCP in (72b). The Special Order Set 1 (SOS1) constraint in (72f) ensures that at most one binary control is active at a time. The inequality and combinatorial constraints described in Section 3 enter the MIOCP in (72c). The limits of the continuous controls u are given in (72d) and the binary constraints for b in (72e). Constraint (72g) ensures that the slack variables s only take positive values and constraint (72h) defines that process noise is considered zero within the MIOCP. The initial state constraint is given in (72i).

4.2 | Description of the MPC algorithm

For solution of OCPs, application of direct methods (*first discretize, then optimize* approach) and especially direct multiple shooting⁴⁴ and direct collocation⁴⁵ is favorable. For discretization of the MIOCP (72), we utilize the fact that typically more control interaction is needed during daytime when operating a solar-driven system. Therefore, we set up a time grid for the control horizon with $t_f = 24$ h with time steps of $\Delta t_d = 15$ min in times between 4:30 and 21:30 and $\Delta t_n = 30$ min between 21:30 and 4:30 to reduce the number of discrete time points, and with this, the size of the resulting MINLP. Since the step size Δt_d might still be too large to successfully control the solar collector temperatures, as the solar irradiation can be subject to fast and large fluctuations (e. g. through movement of clouds) and create need for more frequent updates of P_{psc} and M_{psc} , the first discrete interval of the time grid is further discretized in $n_{t,mpc,s} = 10$ shorter intervals. This results in a time grid with a total of $n_{t,mpc} = 91$ intervals. The discretization is conducted using direct collocation with Lagrange polynomials with Radau collocation points of order 3, cf. Reference 34. To avoid the need for regeneration of the discretization in between subsequent rolling-horizon MPC steps due to changing step length in between two time points caused by the nonequidistant time grid, a time transformation is applied to the ODE right hand side so that the time steps can enter the resulting MINLP as parameters, cf. References 30 and 46.

For controls and time-varying parameters, we assume that their values only change at the discrete time points. Also, different from the description in Section 3, the variables p_{mpsc} , $\dot{m}_{o,hts,b}$, and $\dot{m}_{i,hts,b}$ enter the discretized MIOCP not as states

[¶]Please note that the weighting factors for Δp_{mpsc} , $\Delta \dot{m}_{o,hts,b}$, and $\Delta \dot{m}_{i,hts,b}$ in ω_u need to be set to zero, since these controls can take negative values.

but directly as controls of the system, and the change of these controls is penalized by including the squared difference of the piece-wise constant control values for subsequent time steps in the MINLP objective.

For solution of the resulting MINLPs on real-time suitable time scales, we apply the combinatorial integral approximation (CIA) decomposition approach^{26,27} which has shown good performance regarding solution time and quality in previous studies.^{30,47} The idea of the approach is to first solve a relaxed version of the MINLP with dropped binary constraints, which is a nonlinear program (NLP) further referred to as NLP_{rel} , then to approximate the obtained relaxed binary controls $q \in [0, 1]^{n_b}$ with binary controls $p \in \{0, 1\}^{n_b}$ by solution of a CIA problem,³¹ and afterward to solve the MINLP again with binary controls $b := p$ fixed, which is again an NLP further referred to as NLP_{bin} , to adjust the states x , continuous controls u , and the other remaining optimization variables to the obtained binary solution, cf. Reference 48.

As explained above, the continuous controls should be updated frequently within this application. However, such frequent updates are not necessary for the binary controls, which renders the solution of the complete MINLP for each short term step unnecessary. Also, despite the fact that the decomposition approach can have a drastically reduced solution time compared to general MINLP solvers,⁴⁷ the time spent within the individual solution steps can still be significant, especially for the NLPs.³⁰

Under these considerations, we introduce the algorithm depicted in Figure 8, which is a parallelized algorithm for mixed-integer nonlinear MPC. After generation of an initial guess using a suitable system simulation \bar{f}_{init} for the estimated initial state \hat{x}_{init} of the system, the algorithm is running in two parallel threads. While the thread depicted in the top solves the relaxed MINLP and the CIA problem to obtain updates for the relaxed and approximated binary solution q and p , respectively, the thread depicted on the bottom computes more frequent updates of continuous controls u , states x etc. by repeated solution of NLP_{bin} . After m solutions of NLP_{bin} , the previously used binary controls are replaced with the updated binary approximation p . For the first iteration $k = 0$ of the algorithm, the binary controls for use within NLP_{bin} are provided by the initial guess simulation.

To compensate the delay introduced by the solution time of the NLPs, a method entitled *delay compensation by prediction*⁴¹ is applied. Here, the NLPs are not formulated and solved to generate controls for the current discrete time point $t_{k,i}$ at which the computation started, but for an upcoming discrete time point $t_{k,i+1}$ and applied once this time point is reached. For this, a prediction $\hat{x}_{k,i+1}^+$ of the state for the next relevant discrete time point is required, which is generated by solving a corresponding initial value problem (IVP) $\bar{f}(\cdot)$ for the ODE model f on the corresponding time interval, considering the current state $\hat{x}_{k,i}$ of the system and the controls applied during the time interval. Accordingly, NLP_{rel} and the instance of NLP_{bin} solved at the time point t_m correspond to the first discrete time point $t_{k+1,0}$ of the next iteration $k + 1$ of the algorithm.

Due to the chosen time grid, the scheduled time for one iteration of the total algorithm is $\Delta t_d = 15$ min during day and $\Delta t_n = 30$ min during night. Accordingly, the available time for preparation and solution of one instance of NLP_{bin} is $\Delta t_d / n_{\text{t,mpc,s}} = 90$ s during day and $\Delta t_n / n_{\text{t,mpc,s}} = 180$ s during night, while the available time for preparation and solution

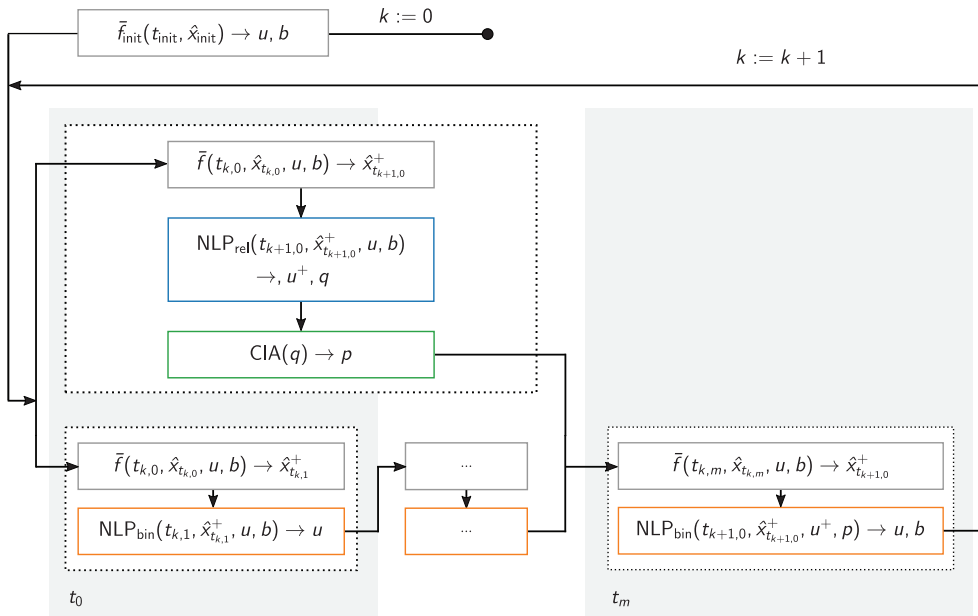


FIGURE 8 Flow chart of the parallelized MPC algorithm

of one sequence of NLP_{rel} and CIA is $((n_{t,mpc,s} - 1)/n_{t,mpc,s})\Delta t_d = 810$ s during day and $((n_{t,mpc,s} - 1)/n_{t,mpc,s})\Delta t_n = 1620$ s during night. Within this study, the preparation time reserved for each problem instance for, for example, data preparation and simulation, is approximately 6 s, the remaining time is available for solution of the problem instance.

4.3 | Implementation of the MPC algorithm

The algorithm implementation is based on Python, while the separate threads are realized using the Python multiprocessing module⁴⁹ and data exchange and synchronization in between processes are realized using blocking queues.⁴⁹

The MINLP is implemented using CasADi⁵⁰ via its Python interface. For this application, preliminary tests showed that using CasADi's SX-type variables results in reduced NLP solution times in comparison to using MX-type variables, since less time is spent for evaluating NLP functions and derivatives. However, utilization of the spline interpolation functionalities³⁵ to depict the solar collector mass flows shown in Section 3.1 requires the use of MX-type variables. But nevertheless, the code generation functionality of CasADi can be used to a priori generate C code for the NLP that contains all functions required by the solver, which can be compiled prior to starting the MPC algorithm and the resulting object later be used (and reused) with the NLP solver. For this application, the generated code was compiled using Clang⁵¹ with optimization level 1 and the resulting object was able to yield function evaluation times comparable to using SX-type variables.

The NLPs within the MPC algorithm are solved using Ipopt⁵² with linear solver MA57.⁵³ Ipopt is configured to use its adaptive barrier parameter update strategy. The CIA problem is solved using pycombina.³⁰ The initial guess simulation is implemented in Modelica and conducted using OpenModelica⁵⁴ via its Python interface OMPython.⁵⁵

The maximum switching and dwell time constraints for the ACM operation modes are considered only in the CIA problem stage of the MPC algorithm and not in the NLP_{rel} stage to avoid further increase of the size of NLP_{rel}. In particular, the AC mode is required to remain active for at least 1 h after activation and inactive for at least 0.5 h after deactivation, while the FC mode is required to remain both active after activation and inactive after deactivation for at least 0.25 h. The maximum amount of allowed switches is determined heuristically from the relaxed solution of the preceding NLP_{rel} stage, however, with a minimum number of three allowed switches per mode.

4.4 | MHE problem formulation and implementation

The relation of states x and associated measurements y is depicted by the measurement function $\Phi(\cdot)$. We assume that the states T_{hts} of the HTS and T_{lts} of the LTS are associated with the temperature sensors T_{hts} and T_{lts} , and the temperature states at the outlet of the solar collector arrays $T_{vtsc,s}$ and $T_{fpvc,s}$ with the sensors T_{vtsc} and T_{fpvc} , respectively. The states $T_{shx,psc,i}$, $T_{shx,psc,n_{shx}}$, $T_{shx,ssc,i}$, and $T_{shx,ssc,n_{shx}}$ are determined via $T_{shx,psc,i}$, $T_{shx,psc,o}$, $T_{shx,ssc,i}$ and $T_{shx,ssc,o}$.

The state of the water side of the FCUs is associated with $T_{fcu,o}$. The air temperature states $T_{r,a}$ of the room are determined from a combination of air room sensors at different heights and locations, similar to the concrete temperature states $T_{r,c}$ which are determined from the sensors attached to the concrete masses.

The current value of the auxiliary state ΔT_{amb} is determined via the corresponding forecast $T_{amb,fc}$ and the ambient temperature sensor T_{amb} . Similarly, the states ΔI_{vtsc} and ΔI_{fpvc} are determined via the forecasts $I_{vtsc,fc}$ and $I_{fpvc,fc}$ and the pyranometer I_g with measurements converted to the orientation of the corresponding collector array's surface.

Using a time grid with $n_{t,mhe} = 20$ equidistant time steps over the past 20 minutes, the MHE problem for estimation of the current system state $\hat{x} = x_{n_{t,mhe}}$ is formulated as

$$\underset{x,w}{\text{minimize}} \quad \sum_{k=0}^{n_{t,mhe}} \|y_k - \Phi(x_k, u_k, b_k, c_k)\|_{\Sigma_y^{-1}}^2 + \sum_{k=0}^{n_{t,mhe}-1} \|w_k\|_{\Sigma_w^{-1}}^2 + \|x_0 - x_{arr}\|_{\Sigma_{arr}^{-1}}^2 \quad (73a)$$

$$\text{subject to } x_{k+1} = \bar{f}(x_k, u_k, b_k, c_k, w_k), \quad k = 0, \dots, n_{t,mhe} - 1, \quad (73b)$$

$$0 \leq w_{\Delta_{a_{vtsc}},k} \leq w_{\Delta_{a_{vtsc}},\max}, \quad k = 0, \dots, n_{t,mhe} - 1, \quad (73c)$$

$$0 \leq w_{\Delta_{a_{fpvc}},k} \leq w_{\Delta_{a_{fpvc}},\max}, \quad k = 0, \dots, n_{t,mhe} - 1. \quad (73d)$$

with Φ the measurement function and y the corresponding measurements at the discrete time points with inverse covariance matrix Σ_y^{-1} , w the additive white process noise with inverse covariance matrix Σ_w^{-1} , and $\|x_0 - x_{\text{arr}}\|_{\Sigma_{\text{arr}}^{-1}}^2$ the arrival cost with inverse covariance matrix Σ_{arr}^{-1} . Function $\bar{f}(\cdot)$ is the solution of an IVP for the ODE model f for a discrete time interval $[t_k, t_{k+1}]$.

Similar to the MIOCP, the MHE problem is implemented using direct collocation and code generation in CasADi. As (73) contains no discrete optimization variables, an application of the decomposition approach is not required and the arising NLPs are directly solved using Ipopt and MA57. Arrival cost updates are conducted using a smoothened extended Kalman filter (EKF), cf. Reference 56. The problem is solved every 60 s in an additional third thread, separate from the MPC loop.

4.5 | Computational hardware, software, and data sources

Both the MPC and the MHE problems are solved on a Fujitsu P920 Desktop PC with an Intel Core i5-4570 3.20 GHz CPU and 16 GB RAM running Debian 9, using Python 3.5, Clang 7, CasADi build 6d29fee,[#]pycombina 0.3.1, and OpenModelica 1.13.2. The forecast data used within this study are retrieved from solcast.com⁵⁷ and updated every hour.

5 | EXPERIMENTAL MIXED-INTEGER NONLINEAR MPC OPERATION

In the upcoming sections, results of experimental operation of the system using mixed-integer nonlinear MPC are presented. In the following, first the experimental setup is described, followed by a presentation and discussion of the experimental results. Finally, the solution times of the algorithm are presented.

5.1 | Setup of the experimental study

To investigate the applicability of mixed-integer nonlinear MPC for the solar thermal climate system, experimental operation of the system has been realized. The results presented in the following were obtained from an operation test on August 1, 2019 from 05:00 to 19:10 UTC. For that day, weather forecasts indicated high solar irradiation and relatively high ambient temperature for a summer day. Especially due to the high availability of driving energy, it was expected that the day would provide beneficial conditions to evaluate the capabilities of the MPC for operating the system at high temperatures and for prevention of overheating.

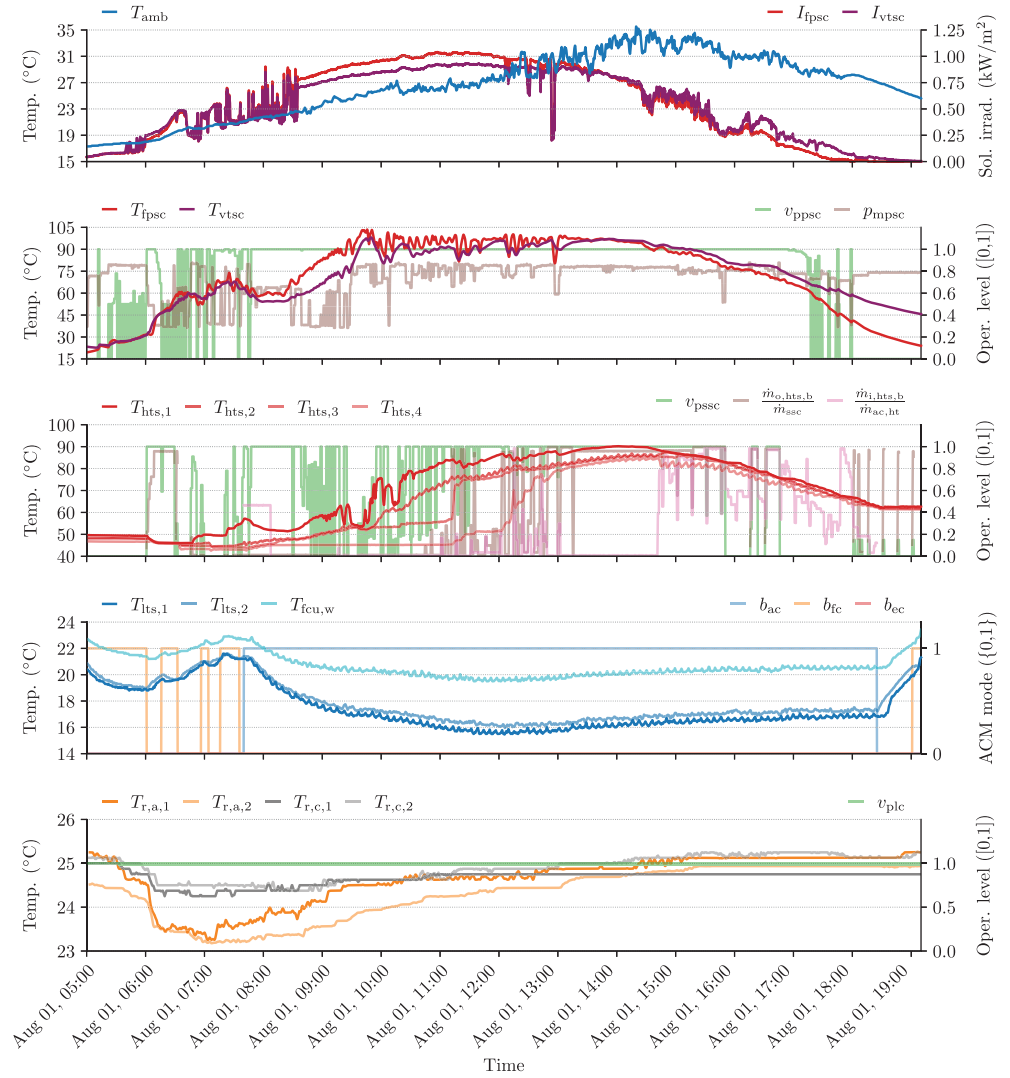
For running the experiment, the MPC was activated in the morning after a night where the climate system was not operating. Due to a longer hot weather period prior to the experiment, both the air and concrete temperature of the building were relatively high, partially exceeding 25°C. Due to that and the high availability of driving energy, it was decided to set the room temperature comfort range for the experiment to a deliberately low range of $[T_{r,a,\min}, T_{r,a,\max}] = [21^\circ\text{C}, 22^\circ\text{C}]$, as even though this room temperatures would not be achieved due to limitations in cooling power, such setting would cause the MPC to aim at maximum cooling power generation. The outdoor blinds of the glass roof of the building were closed during the whole day. The heat input caused by people in the building was very limited as the experiment was conducted during the semester break.

5.2 | Results and discussion of the experimental study

Figure 9 shows the results of the experimental MPC operation. From top to bottom, the plot shows the measured ambient conditions, solar collector temperatures, HTS temperatures, LTS temperatures, and room air and concrete temperatures measured over the considered horizon and corresponding, influencing controls. In the upcoming sections, a detailed explanation and interpretation of the system behavior is given.

[#]At the time of writing, this explicit build of CasADi is required, as it implements all features required for this study for use in combination with the Python multiprocessing module.

FIGURE 9 Temperature measurements and control actions for the system operated using mixed-integer nonlinear MPC on August 1, 2019, from 05:00 to 19:10



The ambient conditions measured during the day of the experiment are shown in the top plot of Figure 9. The solar irradiation throughout the day has been measured using the pyranometer on the roof. While the irradiation profile I_{vtssc} on the VTSC was measured directly, the irradiation I_{fpssc} on the FPSC mounted at 45° angle is computed from the pyranometer measurements using pysolar.⁵⁸ The depicted measurements indicate that, after a partly cloudy morning, the irradiation profile was very stable during noon with high irradiation on the collector surfaces, apart from a few disturbances in the afternoon, until the evening again was partly cloudy. This confirms the expected high availability of solar energy during the day at predominantly stable conditions.

The ambient temperature T_{amb} measured on the roof of the building rose steadily from approximately 18°C in the morning and peaked in the late afternoon at 35°C . Later, T_{amb} decreased again to approximately 25°C at the end of the experiment. The profile shows the expected higher ambient temperature during the day, as well as free cooling potential that could be utilized by the system at the beginning of the day.

5.2.1 | Solar circuits

The second plot from top in Figure 9 shows the measurements for the temperature sensors T_{vtssc} and T_{fpssc} at the outlet of the VTSC and FPSC, respectively. It can be observed that despite the partly fluctuating but high solar irradiation, the MPC is able to achieve high, however slightly fluctuating, collector temperatures close to their defined maximum temperature throughout the major part of the day, which is a desirable result.

Prior to approximately 9:00, an interesting observation can be made where the controller utilizes the solar mixing valve to keep the mass flow through the FPSC low while increasing the flow through the VTSC. Even though T_{fpssc} shows a

higher temperature than $T_{\text{vtsc},s}$, it appears to be more favorable not to realize a higher flow through the FPSC and to avoid temperature alignment of the arrays, which would be the aim of a conventional control approach. As both the area and the heat loss coefficient of the FPSC are bigger compared to the VTSC, the controls identified by the MPC increase the heat dissipation of the system to the environment. One plausible interpretation is that the MPC aims to reduce heat storage during that time, and with this, to prevent overheating of the system later during the day, which would be particularly remarkable.

During a phase of active heating of the collector fields between 09:30 and 10:00, the temperature exceeds the specified maximum by approx. 5 K. However, this temperature is still below the limits at which the EC mode of the ACM is activated by the PLC. In fact, activation of the EC mode was avoided throughout the entire day, and the safety constraints (56)–(58) which ensure that P_{psc} is always in full operation once one collector temperature exceeds 65°C are always fulfilled.

The MPC performance could possibly be further improved by introduction of a more detailed model of the pipe that connects the SHX and the collector fields. Though the volume of one pipe distance from the cellar to the roof contains approximately 0.2 m³ of solar liquid, currently only one temperature state is used for modeling of this distance. Therefore, a more fine-grained depiction of the temperature distribution along the tube using more temperature states could probably improve both temperature constraint satisfaction and reduce the fluctuation of collector temperatures when operating close to their maximum value. However, this increase in the number of states would also increase the solution time for the MINLP, while reliable estimation of the corresponding state values would probably require installation of further temperature sensors.

5.2.2 | High-temperature storage

The middle plot in Figure 9 shows the measurements for the $n_{\text{hts}} = 4$ temperature sensors $T_{\text{hts},k}$, $k = 1, \dots, n_{\text{hts}}$ of the stratified HTS. It can be observed how the MPC actively utilizes the several inlets and outlets of the storage within its control decisions, which is detailed in the following.

Prior to 11:00, the MPC uses mainly the middle outlet $O_{\text{hts},m}$ and middle inlet $I_{\text{hts},m}$ of the HTS. Doing this, it utilizes only the upper part of the stratified HTS for heat exchange with the PSC via SHX, which results in a rapid heating of this part of the storage as illustrated by the sensors $T_{\text{hts},1}$ and $T_{\text{hts},2}$. Due to that, high HT temperatures for ACM operation can be achieved earlier as if the total storage would be heated up, which results in both a longer and more efficient operation of the ACM.

Past 11:00, the MPC first starts to utilize the lower outlet $O_{\text{hts},b}$. By mixing in water from the bottom region of the HTS, the temperature of the solar liquid at the SHX outlet can be reduced more as if only water from the upper region of the HTS was supported to the SSC. This is actively considered to prevent the solar collectors from overheating.

Later during the day and after the peak of solar energy availability, the MPC often fully utilizes the lower outlet $O_{\text{hts},b}$ and lower inlet $I_{\text{hts},b}$. As no storage capacity needs to be held available for reduction of the collector temperatures, the total HTS can be used at that part of the day so that more of the heat energy remaining in the PSC can be extracted.

These observations are particularly remarkable, as they exemplify the advantages of MPC for situational and individual control decisions. While it was not favorable in the morning to use the total HTS but to keep the lower part of the storage at lower temperatures, it is favorable in the afternoon to extract as much energy as possible from the PSC and store it in the HTS. As the optimality of this decision however depends strongly on the expected ambient conditions and differs for other scenarios, it is hard to achieve comparable behavior using a conventional controller based exclusively on current measurements.

5.2.3 | Adsorption cooling machine

As shown in the second plot from the bottom in Figure 9, the ACM is operated in FC mode during the morning when ambient temperature is still comparatively low and it can be observed that the temperature of the LTS is reduced. At the same time, P_{lc} and the FCUs are operated to decrease the room air temperature, as shown in the bottom plot of Figure 9.

Once a sufficiently high temperature in the top of the HTS is reached, the ACM is started and operates in AC mode at comparatively high LT storage temperature and still low ambient temperature, which results in high COP and cooling power of the ACM. This results in a rapid temperature decrease in the LTS. During the day, operation in AC mode continues and the LTS temperature decreases further until approximately 12:00. After that, rising ambient temperatures

and later also decreasing HTS temperatures result in a slight but steady increase of LTS temperatures until the machine is turned off at around 18:30. After that time, the MPC decides to use the remaining cooling energy stored in the LTS, before continuing in FC mode at the end of the experiment when the LTS temperature meets the ambient temperature level again.

Apart from its purpose to provide cooling power, operation of the ACM in AC mode is important for the system functionality itself, as without the machine acting as a heat consumer, emergency cooling of the HTS via the RT or a shutdown of the system due to gasification of the solar liquid might become necessary at some point. Accordingly, surplus of heat during the day and corresponding negative effects can be avoided if the activation time of the ACM is chosen based on the expected solar irradiation over the day instead of fixed HTS temperature set points. In contrast to using MPC, this can hardly be achieved using conventional, set-point and PID-based controllers.

This can be further exemplified on the controllers choice for ACM operation at the end of the day. Though the HTS temperature would still be sufficiently high to drive the ACM in AC mode after 18:30, the MPC decides to utilize FC also before all driving energy in the HTS is used up. In between, ACM operation is paused so that the cooling energy stored in the LTS can be utilized first, as the temperature level for FC utilization is rather high.

Doing this, driving energy is retained in the HTS for an earlier AC start in the upcoming day. Such an earlier start has been scheduled for approximately 5:00 of the upcoming day, as shown in Figure 10 which depicts the predicted system operation for the upcoming 24 h at the end time point of the experiment. While the controller aims to use FC during the night where ambient temperatures are lower, the AC is activated early on the upcoming day, which results in favorable operation conditions for the ACM while generating storage capacity for the solar energy expected during the day.

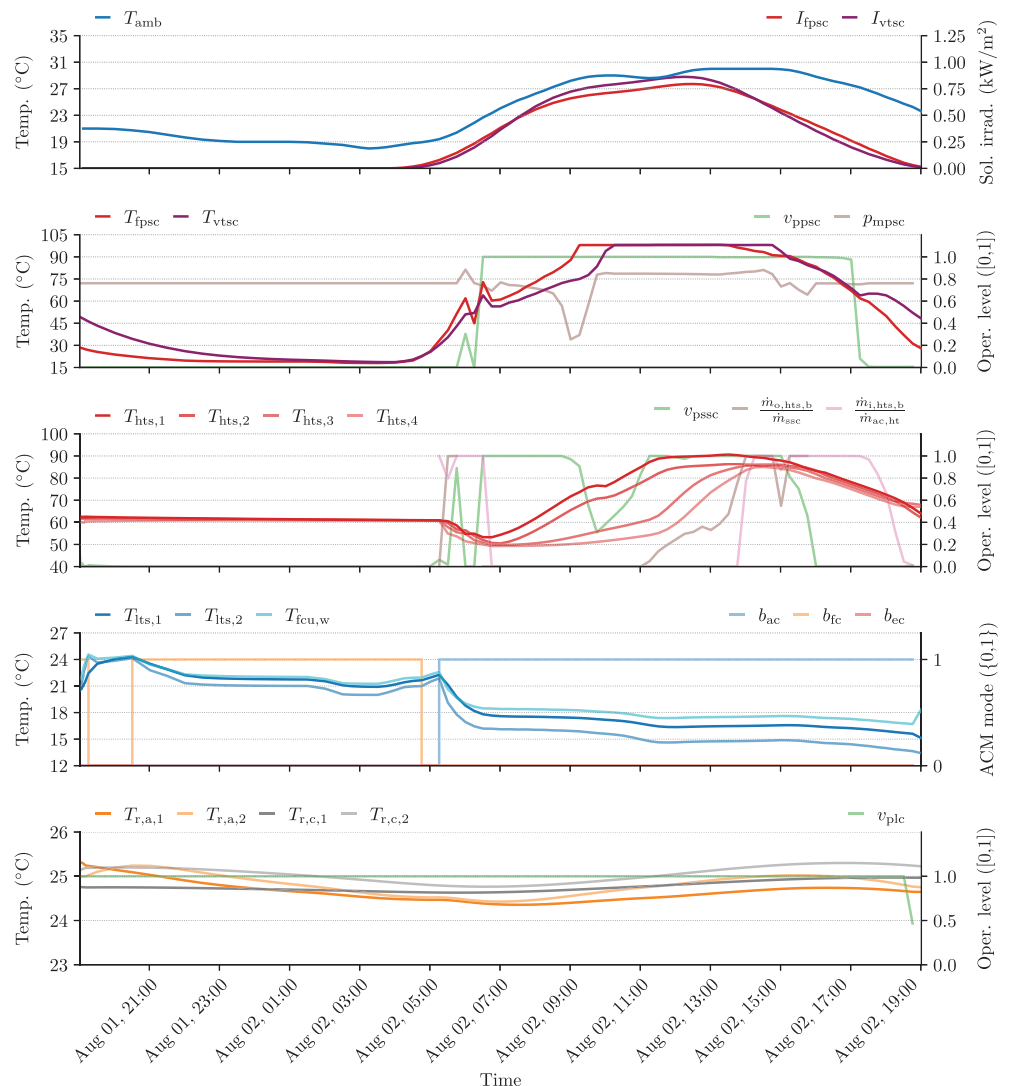


FIGURE 10 Predicted system temperatures and control actions for the upcoming 24 hours on August 1, 2019 at 19:10

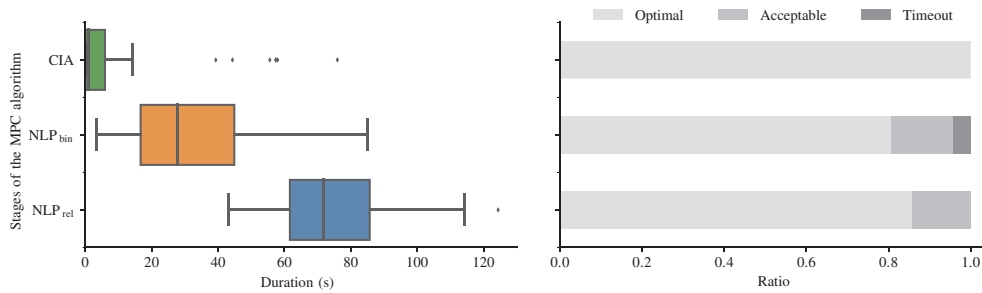


FIGURE 11 Durations and return status of the individual steps of the MPC algorithm for a total of 42 executions of NLP_{rel} and CIA and 416 executions of NLP_{bin}

5.2.4 | Low-temperature circuits and room installations

As expected from the setup of the experiment, the pump P_{lc} and with it the FCUs are operated permanently, due to the relatively high temperatures in the building compared to $T_{r,a,min}$ and $T_{r,a,max}$, which is depicted in the bottom plot in Figure 9.

In the beginning of the day, a major temperature drop of the room air temperatures $T_{r,a,1}$ and $T_{r,a,2}$ can be observed. This is, however, not solely caused by the operation of the climate system alone, but due to major ambient air exchange caused by multiple open windows in the building opened by the faculty staff in the beginning of the day, which were closed again once the ambient temperature achieved a higher level than the room air temperature. This illustrates the high influence of building usage on system operation.

As soon as the windows got closed at around 7:00, the room temperature started to increase again since the concrete temperatures $T_{r,c,1}$ and $T_{r,c,2}$ were still high, which illustrates the strong influence of the heat stored in the concrete mass of the building on the air temperature development. Due to that, the climate system is as expected not capable of driving the room temperatures to the specified comfort region, as the system setup is not capable of providing the required cooling power. However, the climate system is able to prevent further heating of the building and to compensate most of the occurring heat loads, illustrated by the stagnating room temperature development.

5.3 | Runtime of the algorithm

An overview of the runtime of the individual steps of the MPC algorithm and the return status of the solution processes are given in Figure 11. It can be observed that solving NLP_{bin} takes typically less time than NLP_{rel}, which was assumed during algorithm design. More than 95 % of the 416 solutions of NLP_{bin} finished prior to the timeout of approximately 84 s. For all of these finished instances and for all instances of NLP_{rel}, often optimal or at least acceptable solutions have been obtained, so that no problem has been classified infeasible. While the runtime of the CIA is typically much lower than those of the NLPs, several outliers have been registered with an algorithm runtime of up to 75 s. However, also the maximum runtime for both NLP_{rel} and CIA are still far below the maximum possible runtime of approximately 15 min.

6 | CONCLUSIONS AND FUTURE WORK

In this work, we presented a real-life experiment in which we demonstrate the real-time applicability of nonlinear mixed-integer MPC for a solar thermal climate system. For this, we first described a control-oriented nonlinear model of the system. Then, we introduced a parallelized algorithm for mixed-integer nonlinear MPC including a corresponding implementation for the system. Afterward, we presented and discussed the results of real-time experimental operation of the physical system. We have shown that the controller was able to successfully operate the system and actively utilized ACM, pumps, and mixing valves within situational and individual control decisions. The advantages of mixed-integer nonlinear MPC for control of the solar collector fields, active utilization of storage temperature stratifications, and consideration of ACM operation efficiency were highlighted. Finally, we have shown that the solution times of the utilized algorithm and implementations were suitable for real-time control of the system.

Future work should focus on extended tests for MPC operation, including operation on longer time periods and during different weather scenarios and ambient conditions. Improvement of the system model and systematic tuning of problem

and solver parameters could yield further control performance gains. In this regard, comparisons also to other control strategies, such as conventional controllers, linear(ized) MPC strategies, or strategies based on meta-heuristics, could be considered. Also, an extension toward a stochastic MPC approach could be considered, where different forecast variants for upcoming operation conditions could be taken into account simultaneously. Further, if a continuous MPC operation of the system should be facilitated also during cold seasons, the winter operation mode of the system where collected solar heat is used for heating support of the building needs to be included in the system model. In this context, an extension of the current plant configuration by installation of a reversible heat pump could be considered, as an extension of the plant by such an additional switched component could not only yield the possibility for experimental nonlinear mixed-integer MPC applications also during cold seasons, but, however, also allow for a higher number of possible operation modes during summer operation and an increased impact of the cooling system on the building temperatures.

ACKNOWLEDGMENTS

This research was supported by the German Federal Ministry for Economic Affairs and Energy (BMWi) via eco4wind (0324125B) and DyConPV (0324166B), by DFG via Research Unit FOR 2401, by the State Ministry of Baden-Wuerttemberg for Sciences, Research and Arts (Az: 22-7533.-30-20/9/3), by the German Federal Ministry for the Environment, Nature Conservation, and Nuclear Safety (BMU) via WIN4Climate (03KF0094A), by the Reiner Lemoine Stiftung (1581440000956), by INTERREG V Upper Rhine, project ACA-MODES, and Open Access funding enabled and organized by Projekt DEAL.

The forecast data for solar irradiation and ambient temperature used within this work was provided by solcast.com,⁵⁷ whose support of our work we kindly acknowledge.

Further, the authors would like to thank the facility management team at Karlsruhe University of Applied Sciences around Matthias Franke for their support during installation, commissioning, and maintenance of the solar thermal climate system.

Finally, the authors want to thank three anonymous reviewers, whose valuable comments and feedback helped to improve and clarify this manuscript.


DATA AVAILABILITY STATEMENT

Research data are not shared.

ORCID

Adrian Bürger  <https://orcid.org/0000-0003-2740-4526>

Daniel Bull  <https://orcid.org/0000-0002-2391-3967>

Parantapa Sawant  <https://orcid.org/0000-0002-5714-0114>

REFERENCES

- Cominesi SR, Farina M, Giulioni L, Picasso B, Scattolini R. A two-layer stochastic model predictive control scheme for microgrids. *IEEE Trans Control Syst Technol*. 2018;26(1):1-13. <https://doi.org/10.1109/TCST.2017.2657606>.
- Razzanelli M, Crisostomi E, Pallottino L, Pannocchia G. Distributed model predictive control for energy management in a network of microgrids using the dual decomposition method. *Opt Control Appl Methods*. 2020;41:25-41. <https://doi.org/10.1002/oca.2504>.
- Fischer D, Madani H. On heat pumps in smart grids: a review. *Renew Sustain Energy Rev*. 2017;70:342-357. <https://doi.org/10.1016/j.rser.2016.11.182>.
- Zhao Y, Lu Y, Yan C, Wang S. MPC-based optimal scheduling of grid-connected low energy buildings with thermal energy storages. *Energ Build*. 2015;86:415-426. <https://doi.org/10.1016/j.enbuild.2014.10.019>.
- Schirrer A, Brandstetter M, Leobner I, Hauer S, Kozek M. Nonlinear model predictive control for a heating and cooling system of a low-energy office building. *Energ Build*. 2016;125:86-98. <https://doi.org/10.1016/j.enbuild.2016.04.029>.
- Vasallo MJ, Bravo JM. A MPC approach for optimal generation scheduling in CSP plants. *Appl Energy*. 2016;165:357-370. <https://doi.org/10.1016/j.apenergy.2015.12.092>.
- Cojocaru EG, Bravo JM, Vasallo MJ, Marín D. A binary-regularization-based model predictive control applied to generation scheduling in concentrating solar power plants. *Opt Control Appl Methods*. 2019;41:215-238. <https://doi.org/10.1002/oca.2498>.
- Camacho EF, Bordons C. *Model Predictive Control*. Advanced Textbooks in Control and Signal Processing. 2nd ed. London, UK: Springer London Limited; 2007.
- De Coninck R, Helsen L. Practical implementation and evaluation of model predictive control for an office building in Brussels. *Energ Build*. 2016;111:290-298. <https://doi.org/10.1016/j.enbuild.2015.11.014>.
- Oldewurtel F, Parisio A, Jones CN, et al. Use of model predictive control and weather forecasts for energy efficient building climate control. *Energ Build*. 2012;45:15-27. <https://doi.org/10.1016/j.enbuild.2011.09.022>.

11. Qi W, Liu J, Christofides PD. Distributed supervisory predictive control of distributed wind and solar energy systems. *IEEE Trans Control Syst Technol.* 2013;21(2):504-512. <https://doi.org/10.1109/TCST.2011.2180907>.
12. Kuboth S, Heberle F, König-Haagen A, Brüggemann D. Economic model predictive control of combined thermal and electric residential building energy systems. *Appl Energy.* 2019;240:372-385. <https://doi.org/10.1016/j.apenergy.2019.01.097>.
13. Ma J, Qin SJ, Salsbury T. Application of economic MPC to the energy and demand minimization of a commercial building. *J Process Control.* 2014;24(8):1282-1291. <https://doi.org/10.1016/j.jprocont.2014.06.011>.
14. Fischer D, Bernhardt J, Madani H, Wittwer C. Comparison of control approaches for variable speed air source heat pumps considering time variable electricity prices and PV. *Appl Energy.* 2017;204:93-105. <https://doi.org/10.1016/j.apenergy.2017.06.110>.
15. Bürger A, Bohlayer M, Hoffmann S, Altmann-Dieses A, Braun M, Diehl M. A whole-year simulation study on nonlinear mixed-integer model predictive control for a thermal energy supply system with multi-use components. *Appl Energy.* 2020;258:114064. <https://doi.org/10.1016/j.apenergy.2019.114064>.
16. Zafra-Cabeza A, Velarde P, Maestre JM. Multicriteria optimal operation of a microgrid considering risk analysis, renewable resources, and model predictive control. *Opt Control Appl Methods.* 2020;41:94-106. <https://doi.org/10.1002/oca.2525>.
17. Lee Z, Gupta K, Kircher KJ, Zhang KM. Mixed-integer model predictive control of variable-speed heat pumps. *Energy Build.* 2019;198:75-83. <https://doi.org/10.1016/j.enbuild.2019.05.060>.
18. Sangi R, Kümpel A, Müller D. Real-life implementation of a linear model predictive control in a building energy system. *Journal of Building Engineering.* 2019;22:451-463. <https://doi.org/10.1016/j.jobbe.2019.01.002>.
19. Parisio A, Rikos E, Tzamalīs G, Glielmo L. Use of model predictive control for experimental microgrid optimization. *Appl Energy.* 2014;115:37-46. <https://doi.org/10.1016/j.apenergy.2013.10.027>.
20. Fiorentini M, Wall J, Ma Z, Braslavsky JH, Cooper P. Hybrid model predictive control of a residential HVAC system with on-site thermal energy generation and storage. *Appl Energy.* 2017;187:465-479. <https://doi.org/10.1016/j.apenergy.2016.11.041>.
21. Khakimova A, Kusatayeva A, Shamshimova A, et al. Optimal energy management of a small-size building via hybrid model predictive control. *Energy Build.* 2017;140:1-8. <https://doi.org/10.1016/j.enbuild.2017.01.045>.
22. Nocedal J, Wright SJ. *Numerical Optimization.* Springer Series in Operations Research and Financial Engineering. 2nd ed. London, UK: Springer; 2006.
23. Lu Y, Wang S, Sun Y, Yan C. Optimal scheduling of buildings with energy generation and thermal energy storage under dynamic electricity pricing using mixed-integer nonlinear programming. *Appl Energy.* 2015;147:49-58. <https://doi.org/10.1016/j.apenergy.2015.02.060>.
24. Huang Y, Wang W, Hou B. A hybrid algorithm for mixed integer nonlinear programming in residential energy management. *J Clean Prod.* 2019;226:940-948. <https://doi.org/10.1016/j.jclepro.2019.04.062>.
25. Kim JS, Edgar TF. Optimal scheduling of combined heat and power plants using mixed-integer nonlinear programming. *Energy.* 2014;77:675-690. <https://doi.org/10.1016/j.energy.2014.09.062>.
26. Sager S. Reformulations and algorithms for the optimization of switching decisions in nonlinear optimal control. *J Process Control.* 2009;19(8):1238-1247. <https://doi.org/10.1016/j.jprocont.2009.03.008>.
27. Sager S, Bock HG, Diehl M. The integer approximation error in mixed-integer optimal control. *Math Program.* 2012;133(1-2):1-23. <https://doi.org/10.1007/s10107-010-0405-3>.
28. Deng K, Sun Y, Li S, et al. Model predictive control of central chiller plant with thermal energy storage via dynamic programming and mixed-integer linear programming. *IEEE Trans Autom Sci Eng.* 2015;12(2):565-579. <https://doi.org/10.1109/TASE.2014.2352280>.
29. Dan M, Srinivasan S, Sundaram S, Easwaran A, Glielmo L. A scenario-based branch-and-bound approach for MES scheduling in urban buildings. *IEEE Trans Ind Inform.* 2020;16(12):7510-7520. <https://doi.org/10.1109/TII.2020.2978870>.
30. Bürger A, Zeile C, Altmann-Dieses A, Sager S, Diehl M. Design, implementation and simulation of an MPC algorithm for switched nonlinear systems under combinatorial constraints. *J Process Control.* 2019;81:15-30. <https://doi.org/10.1016/j.jprocont.2019.05.016>.
31. Sager S, Jung M, Kirches C. Combinatorial integral approximation. *Math Meth Oper Res.* 2011;73(3):363-380. <https://doi.org/10.1007/s00186-011-0355-4>.
32. Bau U, Baumgärtner N, Seiler J, Lanzerath F, Kirches C, Bardow A. Optimal operation of adsorption chillers: first implementation and experimental evaluation of a nonlinear model-predictive-control strategy. *Appl Therm Eng.* 2019;149:1503-1521. <https://doi.org/10.1016/j.applthermaleng.2018.07.078>.
33. Chang W-S, Wang C-C, Shieh C-C. Experimental study of a solid adsorption cooling system using flat-tube heat exchangers as adsorption bed. *Appl Therm Eng.* 2007;27(13):2195-2199. <https://doi.org/10.1016/j.applthermaleng.2005.07.022>.
34. Biegler L. *Nonlinear Programming.* Philadelphia, PA: Society for Industrial and Applied Mathematics; 2010.
35. Gillis J. Lookup tables in optimization with CasADi and OptiSpline. Paper presented at: Proceedings of the Benelux Meeting on Systems and Control; 2018; Soesterberg, Netherlands. <https://lirias.kuleuven.be/retrieve/497901>.
36. Eicker U. *Solar Technologies for Buildings.* Chichester, England: John Wiley & Sons; 2003.
37. Sawant P, Bürger A, Doan MD, Felsmann C, Pfafferoth J. Development and experimental evaluation of grey-box models of a microscale polygeneration system for application in optimal control. *Energy Build.* 2020;215:109725. <https://doi.org/10.1016/j.enbuild.2019.109725>.
38. Wesselak V, Schabbach T, Link T, Fischer J. *Regenerative Energietechnik.* 2nd ed. Berlin/Heidelberg, Germany: Springer Vieweg; 2013.
39. Löhr Y, Mönnigmann M. Receding horizon heat flow control in domestic buildings - yesterday-based disturbance predictions. Paper presented at: Proceedings of the European Control Conference (ECC), Limassol, Cyprus; 2018:404-409.
40. Jung M, Kirches C, Sager S. On perspective functions and vanishing constraints in mixed-integer nonlinear optimal control. In: Jünger M, Reinelt G, eds. *Facets of Combinatorial Optimization.* Berlin/Heidelberg, Germany: Springer; 2013:387-417.

41. Rawlings JB, Mayne DQ, Diehl MM. *Model Predictive Control: Theory, Computation, and Design*. 2nd ed. Santa Barbara, CA: Nob Hill Publishing; 2017.
42. Kirches C. *Fast Numerical Methods for Mixed-Integer Nonlinear Model-Predictive Control*. Wiesbaden, Germany: Vieweg+Teubner Verlag; 2011.
43. Bürger A. stcs-mimpc: a demo implementation of a mixed-integer nonlinear model predictive control algorithm for the solar thermal climate system at Karlsruhe University of Applied Sciences; 2020. <https://github.com/adbuerger/stcs-mimpc>. Accessed October 12, 2020.
44. Bock HG, Plitt KJ. A multiple shooting algorithm for direct solution of optimal control problems. *IFAC Proc Vols*. 1984;17(2):1603-1608. [https://doi.org/10.1016/S1474-6670\(17\)61205-9](https://doi.org/10.1016/S1474-6670(17)61205-9).
45. Tsang TH, Himmelblau DM, Edgar TF. Optimal control via collocation and non-linear programming. *Int J Control*. 1975;21(5):763-768. <https://doi.org/10.1080/00207177508922030>.
46. Gerds M. A variable time transformation method for mixed-integer optimal control problems. *Opt Control Appl Methods*. 2006;27(3):169-182. <https://doi.org/10.1002/oca.778>.
47. Bürger A, Zeile C, Altmann-Dieses A, Sager S, Diehl M. An algorithm for mixed-integer optimal control of solar thermal climate systems with MPC-capable runtime. Paper presented at: Proceedings of the European Control Conference (ECC), Limassol, Cyprus; 2018:1379-1385.
48. Jung M. *Relaxations and Approximations for Mixed-Integer Optimal Control* [PhD dissertation]. Interdisciplinary Center for Scientific Computing, Heidelberg University; 2013.
49. Python software foundation multiprocessing – process-based parallelism; 2019. <https://docs.python.org/3/library/multiprocessing.html>. Accessed August 13, 2019.
50. Andersson JA, Gillis J, Horn G, Rawlings JB, Diehl M. CasADi: a software framework for nonlinear optimization and optimal control. *Math Program Comput* 2019;11(1):1–36. <https://doi.org/10.1007/s12532-018-0139-4>, 1.
51. Clang: a C language family frontend for LLVM; 2019. <http://clang.llvm.org>. Accessed June 10, 2019.
52. Wächter A, Biegler LT. On the implementation of an interior-point filter line-search algorithm for large-scale nonlinear programming. *Math Program*. 2006;106(1):25-57. <https://doi.org/10.1007/s10107-004-0559-y>.
53. HSL A collection of Fortran codes for large scale scientific computation; 2019. <http://www.hsl.rl.ac.uk>. Accessed May 17, 2019.
54. OpenModelica; 2017. <https://www.openmodelica.org>. Accessed June 10, 2019.
55. Lie B, Bajracharya S, Mengist A, et al. API for accessing OpenModelica models from python. Paper presented at: Proceedings of the 9th EUROSIM Congress on Modelling and Simulation, Oulu, Finland; 2016.
56. Grrbach F, Hol JD, Zandbergen R, Verschueren R, Bellusci G, Diehl M. On the effect of stabilization methods for quaternion invariants on the uncertainty in optimization-based estimation. *IFAC-PapersOnLine*. 2018;51(25):116-121. <https://doi.org/10.1016/j.ifacol.2018.11.091>.
57. Solcast Global solar irradiance data and PV system power output data; 2019. <https://solcast.com/>. Accessed June 12, 2019.
58. Stafford B. pysolar; 2018. <https://doi.org/10.5281/zenodo.1461066>, last Accessed August 15, 2019.

How to cite this article: Bürger A, Bull D, Sawant P, et al. Experimental operation of a solar-driven climate system with thermal energy storages using mixed-integer nonlinear model predictive control. *Optim Control Appl Meth*. 2021;42:1293–1319. <https://doi.org/10.1002/oca.2728>